The Pennsylvania State University

The Graduate School

CONTROL-ORIENTED MODELING, STATE-OF-CHARGE, STATE-OF-HEALTH, AND PARAMETER ESTIMATION OF BATTERIES

A Dissertation in

Mechanical Engineering

by

Zheng Shen

Submitted in Partial Fulfillment
of the Requirements
for the Degree of

Doctor of Philosophy

August 2013

ProQuest LLC.
789 East Eisenhower Parkway
P.O. Box 1346
Ann Arbor, MI 48106 - 1346

The dissertation of Zheng Shen was reviewed and approved* by the following:

Chris D. Rahn
Professor of Mechanical Engineering
Dissertation Advisor, Chair of Committee

Asok Ray
Distinguished Professor of Mechanical Engineering

Constantino Lagoa
Professor of Electrical Engineering

Donghai Wang
Assistant Professor of Mechanical Engineering

Karen A. Thole
Professor of Mechanical Engineering
Head of the Department of Mechanical and Nuclear Engineering

*Signatures are on file in the Graduate School

Abstract

Batteries are excellent energy storage devices for many applications, such as renewable energy consumer electronics, smart grids, Hybrid Electric Vehicles (HEVs), and Electric Vehicles (EVs). Among major battery chemistries, Lead (Pb)-Acid batteries are a low-cost power source for applications ranging from hybrid and electric vehicles (HEVs) to large-scale energy storage. Lithium-Ion (Li-Ion) batteries are also widely used in multiple applications such as HEV and EV to supply power to motors because of their high energy and power density and low weight. This research addresses four important problems for efficient utilization of large-scale battery systems: control-oriented modeling, State-Of-Charge (SOC) estimation, State-Of-Health (SOH) estimation, and parameter estimation. Lead-Acid batteries are investigated in the areas of modeling and model-based SOC/SOH estimation. Solid phase diffusivity of a Li-Ion cell is measured as a study of battery parameter estimation.

Efficient simulation, design and management systems require the development of low order but accurate models. Previous efforts to manage battery systems are based on equivalent circuit models, which are low-order models using an equivalent circuit to approximate the battery's response. These models do not describe the underlying electrochemical processes taking place in the battery. At the other end of the spectrum, it is also found that while full order first principles models provide reliable prediction and comprehensive understanding on multiple variables of interest (i.e, voltage, ion diffusion, potential distributions across cells), they are often computationally difficult and costly to solve, since they involve complicated coupled nonlinear partial differential equations (PDEs).

In this research, we develop a reduced-order Lead-Acid battery model from first principles using linearization and the Ritz discretization method. The model, even with a low-order discretization, accurately predicts the voltage response to a dynamic pulse current input and outputs spatially distributed variables of interest.

As an efficient first principles model, the Ritz model makes an excellent candidate for Battery Management System (BMS) model design. Also, a dynamic averaged model is developed from the Ritz model and realized by an equivalent circuit. The circuit resistances and capacitances depend on electrochemical parameters, linking the equivalent circuit model to the underlying electrochemistry of the first principles model.

Among those built-in functionalities of the BMS in a HEV, the State-Of-Charge (SOC) estimation is crucial. SOC is the overall remaining charge in percentage inside a defined unit (cell, battery, module, or battery pack.). For an electric vehicle, the SOC is similar to the remaining fuel for a vehicle powered by internal combustion engine. State-Of-Charge (SOC) estimation for Valve-Regulated Lead-Acid (VRLA) batteries is complicated by the switched linear nature of the underlying dynamics. A first principles nonlinear model is simplified to provide two switched linear models and linearized to produce charge, discharge, and averaged models. Luenberger and switched SOC estimators are developed based on these models and propogated using experimental data. A design methodology based on Linear Matrix Inequalities (LMIs) is used in the switched SOC estimator design to obtain a switched Luenberger observer with guaranteed exponential stability. The results show that estimation errors are halved by including switching in the observer design.

To fully utilize a Lead-Acid cell also requires real-time estimates of its State-Of-Power (SOP) and State-Of-Health (SOH) to efficiently allocate power and energy amongst the cells in a pack. SOP and SOH are inversely and directly proportional to cell resistance and capacity, respectively. In this research, the Least Squares Method estimates the coefficients of a second order transfer function using experimental voltage and current data from new, aged, and dead Valve Regulated Lead-Acid batteries. The coefficients are explicitly related to the cell ohmic resistance, capacity, charge transfer resistance, and double layer time constant using a fundamental model of the cell. The ohmic resistance estimate increases monotonically with age, providing an estimate of SOP. The capacity estimate decreases monotonically with age, matching the actual capacity loss for aged cells. Finally, the voltage estimate error can be used as a SOH/SOP estimator and quantify the reliability of the parameter estimates. The first pulse after a long rest period shows the highest estimation error.

In battery systems, the parameters often vary with SOC, SOH, and operating conditions. Accurate and fast battery parameter measurement methods are desirable in many applications. Solid phase diffusivity D_s is one of the first parameters to be measured in a new Lithium-Ion cell design because it dominates the electrochemical kinetics. Amongst the D_s measurement methods, the Galvanostatic Intermittent Titration Technique (GITT) is easy to implement and univerally

accepted as the standard for diffusivity measurement. The accuracy of GITT, however, has not been reported, because there is no direct measurement method of D_s. In this research, we develop a Least Squares Galvanostatic Intermittent Titration Technique (LS-GITT) that uses all of the voltage data from a GITT test to optimally tune the diffusivity in a reduced order solid phase diffusion model. The accuracy of the GITT and LS-GITT are evaluated using voltage predication error RMS. Based on experimental results from a NCM half cell, LS-GITT is more accurate than GITT, sometimes by several orders of magnitude. LS-GITT gives results accurate to 1 mV RMS from 15% - 100% SOC while GITT provides that level of accuracy over less than half that range. Neither technique provides accurate D_s measurements below 10% SOC.

Table of Contents

List of Figures

List of Tables

Acknowledgments

I would like to express my gratitude to my advisor Dr. Chris D. Rahn for the useful comments, remarks, engagement, and guidance through the learning process of this dissertation. Furthermore, I would like to thank all my Ph.D. committee members, Dr. Lagoa, Dr. Ray, Dr. Wang, and Dr. Sinha for helping me with the topic as well for the support on the way. Also, I would like to thank my labmates, especially Jun Gou, Chris Ferone, Chris Melville, and Lei Cao, who have willingly shared their precious time and effort during the theoretical development and experiments. I would like to thank my loved ones, especially my parents Shen Yulan and Kuang Yanlan, who have supported me throughout entire process, both by keeping me harmonious and helping me putting pieces together. I will be grateful forever for your love. Also, Xie Xie Zuzhi&XiaoGu, LaoDuan&Taozi, Li Yue&Qunzhu, Zhu Bin&YeShuai for the godsend friendship, it's been so wonderful to have you around through the past 4 years.

Chapter 1

Introduction

Rechargeable batteries such as Lead-Acid and Lithium-Ion batteries have been widely used in both industry and consumer products because of their high reliability, energy efficiency, and specific energy density compared to other energy storage devices [1, 2, 3].

In large-scale battery systems like those for hybrid and electric vehicles [2, 4], model-based Battery Management Systems (BMS) are critical for optimal utilization and cycle life extension. The BMS relies on accurate estimates of the battery usage and health status based on the measured input current and output voltage to help control and manage the battery for maximum energy efficiency and life. Hence, computationally easy and accurate battery models are desired for estimation and control functionalities in an advanced BMS.

Previous researchers have proposed many battery models. Generally, these models are devided into two categories: first principles models and equivalent circuit models. First principles models are based on electrochemistry, which can accurately reflect the chemical, heating, and diffusion processes within a battery. Nevertheless, their complex expression and high computational cost make the first principles model unamenable for implementation in the BMS. Equivalent circuit models are efficient enough for the BMS, which are circuits approximating battery's current/voltage behavior using electrical components such as capacitor, resistor, and voltage source. However, equivalent circuit models fail to provide full understanding about some of the key battery mechanisms such as the chemical process. Combining the merits of the two model types, reduced order first principles models

are hence proposed, providing an excellent candidate for the BMS. For example, reduced-order Lithium-Ion battery models are proposed in [5] and [6]. Widely used model order reduction techniques are: Integral Method Approximation [7, 8, 9], Ritz method [7, 10], Finite Element Method (FEM) [11, 12], Finite Difference Method [7, 13], and Padé Approximation Method (PAM) [14, 15]. In this dissertation, we choose the Ritz method to generate a reduced order Pb-Acid battery model from an electrochemical model.

The reduced-order Ritz model can be conveniently used to estimate multiple system variables like State-Of-Charge (SOC) because of its state space model expression. Indicating the remaining charge in a battery system, the knowledge of SOC helps us to make the best of batteries, which can be calculated from the state variables of the Ritz model. One property that distinguishes Pb-Acid battery from most of the other battery types is the abrupt switching of system parameters between charge and discharge. This switching characteristics complicates the SOC estimator design, because the stability of a switched system can not be simply guaranteed by stabilizing every subsystem in it. Hence, in this research, an Switched Luenberger Estimator design technique based on Linear Matrix Inequalities (LMIs) is applied to produce a stable switched SOC estimator under any given mode switching. By comparing the SOC estimation results based on various models, mode switching is proved to be worth taking into account when designing an accurate SOC estimator for Lead-Acid batteries.

State-Of-Health (SOH) estimation is also critical for Battery Management Systems (BMS) that are dedicated to take full advantage of large battery systems. The knowledge of SOH is helpful for battery replacement and optimal utilization so as to extend the cycle life of battery packs. Battery impedance measurement, coup de fouet, parameter estimation methods are major SOH estimation methods for Lead-Acid batteries. A SOH estimation method is proposed that identifies key SOH-related battery parameters using Least Squares Method (LSM). For Lead-Acid batteries, model identification error, i.e., deviation from second-order system is found to be a sensitive SOH indicator that potentially allows SOH estimation at early stages of battery degradation.

Solid phase diffusivity (D_s) determines the dominant pole of Lithium-Ion (Li-Ion) battery dynamics. The accurate measurement of D_s is crucial for modeling

and understanding of the diffusion process. Galvanostatic Intermittent Titration Technique (GITT) is one of the D_s measurement methods that are widely used and universally accepted. We develop a new D_s measurement method, the Least Squares Galvanostatic Intermittent Titration Technique (LS-GITT) by applying the Least Squares Method (LSM) to the voltage and current data of a GITT test and compare the D_s estimates with GITT. The accuracy of the two methods are evaluated using voltage predication error RMS, which shows that the results of LS-GITT are more reliable in a wide range of State-Of-Charge (SOC).

In this chapter, we introduce Pb-Acid battery modeling and related model order reduction methods, SOC and SOH estimation methods for a Pb-Acid battery, solid phase diffusivity measurement for a Li-Ion cell. At the end of this chapter, an overview of this dissertation is provided.

1.1 Pb-Acid Battery Modeling

Invented in 1859 by French physicist Gaston planté, lead-acid batteries are the oldest secondary (rechargeable) battery type. The lead-acid battery can supply very high surge current (> 100A), so it has a relatively high power density (about 220W/Kg at 80% of DOD, better than Ni-MH batteries) in spite of its low energy density (about 166 Wh/Kg). Since created, it has been one of the most popular batteries which maintains 40% - 45% of the battery market, primarily due to its low cost. Most of the world's lead-acid batteries are automobile starting, lighting and ignition (SLI) batteries. Lead-Acid batteries are also the predominant chemistry for stop-start microhybrids that have improved fuel efficiency and reduced carbon and pollutant emission. Lead-Acid batteries provide low-cost energy storage with good power density and safety. They also provide an economical and promising choice for powering HEV due to its high round-up efficiency (75% - 80%). The technology of lead-acid battery industry has been progressing and producing new models. First appeared in 1970s, Valve-Regulated Lead-Acid batteries immobilize electrolyte in gel and prevent acid from spilling, leaking and causing danger.

Figure 1.1 shows a schematic diagram of a lead acid cell, which is divided into 3 domains from left to right: the positive electrode, the separator, and the negative electrode. For Absorptive Glass Mat (AGM) VRLA batteries, positive and

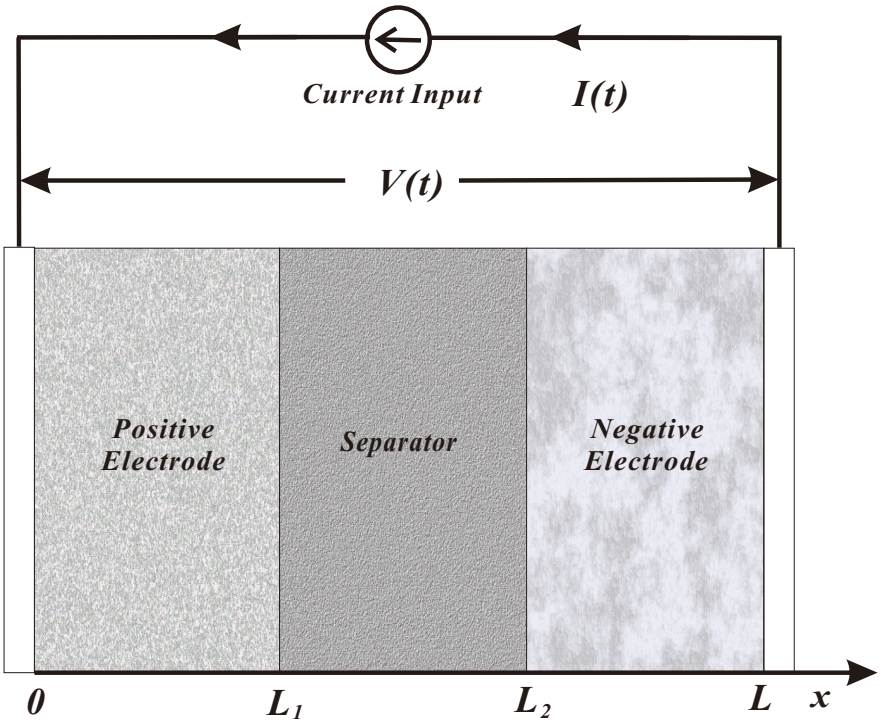

Figure 1.1. Schematic diagram of a lead-acid cell

negative electrodes are plates made of porous solid mixtures of reactants (positive electrode: lead sulfate ($PbSO_4$) and lead dioxide (PbO_2). negative electrode: lead sulfate ($PbSO_4$) and lead (Pb)) saturated in sulfuric acid (H_2SO_4). Separators made of dielectric material insulate postive and negative electrodes physically, which prevent short circuit in solid phase while allowing free electrolyte flow and ion diffusion to keep the electrolyte neutral.

The main electrochemical reactions in the positive electrode of a Pb-Acid battery [16] are

$$PbO_2 + HSO_4^- + 3\,H^+ + 2\,e^- \underset{\text{charge}}{\overset{\text{discharge}}{\rightleftharpoons}} PbSO_4 + 2\,H_2O, \tag{1.1}$$

and the negative electrode,

$$Pb + HSO_4^- \underset{\text{charge}}{\overset{\text{discharge}}{\rightleftharpoons}} PbSO_4 + H^+ + 2\,e^-. \tag{1.2}$$

The reversibility of electrochemical reactions makes lead acid batteries recharge-

Table 1.1. Comparison of discretization methods

Method	Efficiency	Complexity
Ritz Method (AM)	High	Medium
Integral Method Approximation (IMA)	High	Low
Finite Element Method (FEM)	Medium	Medium
Finite Difference Method (FDM)	Low	Low
Padé Approximation Method (PAM)	High	Medium

able. Lead sulfate and water are converted into lead, lead dioxide, and sulfuric acid under charge, and the reactions go reversely under discharge.

Many Pb-Acid battery models have been proposed by researchers. First principle battery models [16, 17, 18, 19, 20, 21] can accurately predict the battery response to any input and provide physical outputs such as acid concentration and electrical potential distributions in the solid and electrolyte phases. These models are usually boundary value problems consisting of coupled partial differential equations that are difficult to solve. Equivalent circuit models [4, 22, 23, 24, 25] are concise, computationally easy and can match experiment results well in many cases. Electrochemical processes are approximated using circuits, and these equivalent circuits with diverse complexity are designed for various purposes with different accuracy requirements. However, equivalent circuit models include no first principles variable like acid concentration and potential distributions so the results can be hard to interpret and understand.

Solutions to coupled partial differential equations in a first principles model are continuous but they can be approximated by discrete points in the solution spaces, so model order reduction can be achieved using discretization methods. Efficient discretization methods are more desirable for battery model order reduction, which means the same accuracy can be achieved with lower model orders.

A variety of discretization methods have been applied to batteries and similar problems in heat conduction, including the Integral Method Approximation [7, 8, 9], Ritz method [7, 10], Finite Element Method (FEM) [11, 12], Finite Difference Method [7, 13], and Padé Approximation Method (PAM) [14, 15]. These methods are studied and summarized in [26] and their characteristics are shown in Tab. 1.1.

Among these methods, the Ritz method is found to be an excellent candidate for VRLA battery modeling, because it is highly efficient and not so difficult for

modeling. Moreover, by choosing Fourier series as its admissible basis functions, most of the boundary conditions for a three-domain VRLA battery can be automatically satisfied.

1.2 State-Of-Charge Estimation

State-Of-Charge (SOC) is defined as the percentage of the maximum charge that remains in the battery [27], or

$$SOC\left(t\right)=\frac{C_r\left(t\right)}{C}=SOC\left(0\right)+\frac{1}{C}\int_0^t I\left(\tau\right)d\tau, \tag{1.3}$$

where $I\left(t\right)$ is the current (>0 for charge), the nominal capacity of the battery C is the maximum ampere-hours that can be drawn from the fully charged cell at room temperature and a C/30 rate, and the remaining capacity $C_r\left(t\right)$ is the ampere-hours that can be drawn from the battery starting from the current time t, at room temperature and at a C/30 rate.

For battery packs used in EVs, SOC is similar to the remaining fuel percentage for a vehicle powered by an internal combustion engine, which is a critical battery usage variable that must be estimated by a BMS. SOC cannot be directly measured but several estimation methods have been developed [28, 29]. The Current Counting Method [30] and Voltage Lookup Method, for example, are widely used. The Current Counting Method is based on Eq. (1.3) and estimates the current SOC by measuring and integrating the dynamic current input. However, one must know the initial SOC and noise in the current sensor can accumulate error with time and cause SOC drift. If the battery has been at rest for several hours then $SOC\left(0\right)$ can be determined from the Open Circuit Voltage (OCV). In dynamic operation there may not be opportunities to correct SOC drift.

Alternatively, one can use the measured voltage in dynamic operation to estimate SOC. OCV has a empirically determined relationship with SOC and the Voltage Lookup Method uses this empirical function on low-pass-filtered voltage data. The Voltage Lookup Method fails to take into account the influence of the input current on the output voltage of a battery, so it is inaccurate during dynamic operation and high current charge/discharge.

The specific gravity of the electrolyte in Pb-Acid batteries is directly related to SOC and can be measured in flooded Lead-Acid cells [31]. In most modern Pb-Acid cells (*e.g.*, Valve Regulated Lead-Acid (VRLA)), the electrolyte is held in Absorbent Glass Mat (AGM) or a gel preventing the use of this method.

The Kalman filter is one of the most widely used techniques for SOC estimation and was used with equivalent circuit battery models by Plett [31, 32, 33]. Vasebi *et al.* [4, 34] designed a VRLA SOC estimator based on an equivalent circuit model using an Extended Kalman Filter. White *et al.* [35, 36, 37] developed SOC estimators using Extended Kalman filtering and Unscented Kalman Filtering based on a reduced-order physics-based Li-Ion battery model.

Experimental results show that the VRLA battery has different dynamics for charge and discharge. A physics-based model using a Ritz discretization [38] includes this effect by having separate linear subsystems for charge and discharge. The model switches between the 2 linear subsystems according to a switching law that depends on the state, making it a switched linear system [39, 40]. State estimation of switched linear systems can often be achieved with a switched Luenberger observer [41].

1.3 State-Of-Health Estimation

To fully utilize a battery pack requires a Battery Management System (BMS) that estimates the the State-Of-Power (SOP) and the State-Of-Health (SOH) of all the cells in the pack. SOH is usually defined as the battery capacity (Ah) divided by the initial capacity [3], a measure of the maximum energy that can be stored in the cell. SOP is inversely proportional to ohmic resistance. The cell impedance as a whole rises with age, reducing the maximum power the cell can provide. The degradation mechanisms that cause capacity fade and impedance rise in Lead-Acid batteries include grid corrosion, water loss, sulfation, active material degradation, and separator metalization [42, 43]. Capacity measurement, impedance measurement, parameter estimation, and coup de fouet methods have been used for SOH estimation. Capacity measurement requires slow, full discharge to 0% State-Of-Charge (SOC) followed by a slow, full charge to 100% SOC. This is impractical for most applications but may be used for plug-in or purely electric vehicles that

see wide-ranging SOC during normal operation. Battery impedance measurement, widely used in industry, employs dedicated hardware and/or software to directly measure either DC or AC resistance of the battery [44, 45]. Battery impedance increases as the battery ages and the measured impedance can be correlated to SOH. The cost and invasiveness of impedance measurement prevent its use in most applications. Coup de fouet [46, 47] is observed in Lead-Acid batteries that have been fully charged, rested and then pulse discharged. During the first discharge pulse, the voltage dips, increases, levels off at a plateau voltage and then decreases steadily. The voltage dip or undershoot has been shown empirically to be proportional to the capacity (SOH) of the battery [48, 49]. The electrochemical mechanism behind coup de fouet is still not understood [46] and the requirement of full charge followed by rest limits its utility. Parameter estimation methods are promising in dynamic applications such as Hybrid Electric Vehicles (HEVs) because SOH can be estimated from the available current and voltage measurements at reasonable sampling rates (*e.g.* 1 Hz). The parameter estimates are for a specific simplified model of the cell electrochemistry, so the estimated parameters are explicitly related to the geometric, material, and electrochemical parameters of the underlying model. Thus, changes in the parameter estimates can be explicitly correlated to specific degradation mechanisms and emperically correlated to SOH. A variety of parameter estimation methods, including Subpace Identification [50, 51], Kalman Filtering [33, 52], Fuzzy Logic [53], and Least Squares [54], have been applied to Lithium-Ion [36, 54], Ni-MH [33], and Lead-Acid [50, 52] batteries. The Least Squares Method (LSM) [55] is used in the present work because of its simplicity, computational efficiency, and guaranteed convergence. LSM is for a linear, time-invariant model and the parameter estimates are the numerator and denominator polynomial coefficients of the impedance transfer function that optimally fit the time-domain current and voltage data. In [54], this method is used to estimate the coefficients of a reduced order Lithium Ion battery model [56] and track the evolution of multiple parameters, including the capacity, diffusion time constant, and impedance.

1.4 Solid Phase Diffusivity Measurement for Li-Ion Cells

Lithium-Ion batteries are excellent energy storage devices for many applications, such as renewable energy consumer electronics, Hybrid Electric Vehicles (HEVs), and Electric Vehicles (EVs), due to their high energy and power density. In dynamic operations, the kinetic behavior of electrode materials dictates the cell response and performance. For most Lithium-Ion chemistries and cell designs, solid phase diffusivity (D_s) dominates the electrochemical kinetics because $\mathbf{Li}^+$ intercalation is the slowest process during charge/dishcarge of the cell. To accurately model the response of a Lithium-Ion cell, D_s must be accurately measured. Solid phase diffusivity is one of the first parameters to be measured in a new cell design because it directly influences the cell power performance. Diffusivity also varies with temperature, State of Charge (SOC), and electrolyte concentration [57]. Thus, the development of fast, reliable, and accurate D_s measurement has been a focus of researchers for many years. Many D_s measurement methods, such as Potentiostatic Intermittent Titration Technique (PITT) [58, 59, 60], Galvanostatic Intermittent Titration Technique (GITT) [57, 61, 62, 63], Electrochemical Impedance Spectroscopy (EIS) [64, 65], and Cyclic Voltammetry (CV) [66, 67], have been used by previous investigators. GITT, because of its solid theoretical foundation and convenient implementation, is widely used and the results are well accepted. GITT uses time-domain voltage data resulting from a prescribed, low C-rate, long rest time current discharge pulse train. Solid phase diffusivities are calculated from the voltage response transients and a plot of D_s versus SOC is generated. The GITT D_s measurement is based on a simplified analytical solution to the fundamental electrochemical equations, providing a firm theoretical foundation [61]. GITT assumes diffusion occurs in a thin layer on the surface of the solid phase material. This assumption requires a short time duration τ of the discharge pulses ($\tau \ll L_s^2/D_s$), where L_s is the characteristic dimension of the solid phase material. The low C-rate coupled with the short pulse time and long rest period mean that an accurate GITT test may take hours to even days to produce an entire D_s versus SOC curve. The final problem with the traditional GITT test is that the accuracy of D_s measurement is unknown. Orders of magnitude differ-

ences in D_s measurement for the same chemistry can be found in the literature [68]. Are the D_s measurement variations with SOC, for example, real on simply artifacts of the GITT test? Certainly, one can perform an uncertainty analysis using the GITT equations but the accuracy of the underlying model that produces the GITT equations has never been quantified.

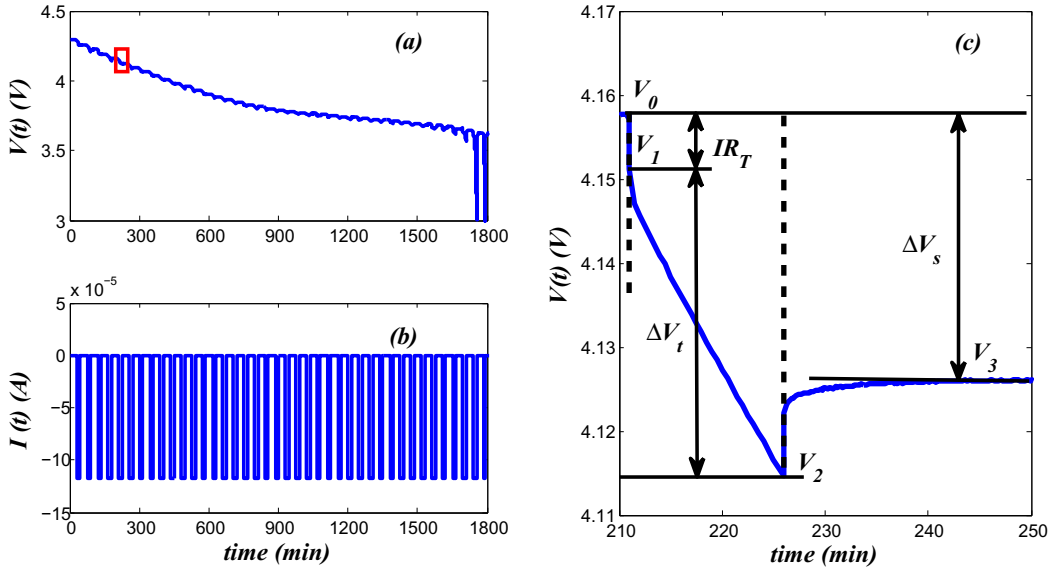

Figure 1.2. GITT data for a NCM coin cell: (a) Voltage, (b) Current, (c) Zoomed-in voltage corresponding to box in (a) (dashed lines delineate start and end of discharge pulse)

Figure 1.2 shows an example GITT test for a coin cell with a Nickel Cobalt Manganese (NCM) [57] positive electrode and a metal Lithium negative electrode. Prior to the test, the cell is fully charged and rested for 1 hr. The GITT current input consists of 40 discharge pulses at 0.1C ($I_0 = 0.00012$ A). Each pulse lasts 15 minutes followed by 30 minutes of rest. After each pulse, the SOC has decreased by 2.5%, so the battery is completely discharged ($SOC = 0\%$) at the end of the test. Applying the GITT measurement methodology to each pulse produces 40 points on the SOC curve. The negative electrode material of the coin cell produces negligible overpotential so the GITT test measures the diffusivity of $\mathbf{Li}^+$ in the NCM cathode.

Figure 1.2 (c) shows the zoomed-in voltage data of one discharge pulse at 92.5% SOC. The cell voltage quickly decreases from V_0 to V_1 due to the total resistance R_T (ohmic and charge transfer resistances), slowly decreases to V_2 due

to the transport of $\mathbf{Li}^+$ in the solid phase, and then when the current is removed, the voltage increases as the $\mathbf{Li}^+$ concentration evenly distributes throughout the solid phase to produce the steady-state, post-discharge voltage V_3. The voltage drops ($\Delta V_s = V_0 - V_3$ and $\Delta V_t = V_1 - V_2$) are calculated from the four voltage measurements V_0, ..., V_3. The GITT D_s measurement is calculated from only four, often hand-picked, data points from what could be hundreds if not thousands of data points in the voltage response, depending on the sample rate. V_1, inparticular, is very sensitive to the sample rate and high frequency, unmodeled dynamics.

The diffusivity is calculated from

$$D_s = \frac{4}{\pi\tau}\left(\frac{n_M V_M}{S}\right)^2\left(\frac{\Delta V_s}{\Delta V_t}\right)^2, \tag{1.4}$$

where n_M and V_M are the molar mass (mol) and volume (cm^3/mol) of the active material, respectively, S is the cell interfacial area, and τ is the time duration of the pulse. For the NCM cathode, we assume that the solid phase consists of spherical particles with radius R_s, so Eq. (1.4) becomes:

$$D_s = \frac{4}{\pi\tau}\left(\frac{R_s}{3}\right)^2\left(\frac{\Delta V_s}{\Delta V_t}\right)^2. \tag{1.5}$$

Eq. (1.5) points out one final limitation of the GITT diffusivity measurement. Phase change materials such as lithium iron phosphate, lithium titanium oxide, and even graphite (present in almost all Lithium-Ion cells) have $\Delta V_s \approx 0$ due to flat Open Circuit Voltage (OCV) versus SOC curves. Eq. (1.5) predicts $D_s \approx 0$ for these materials which is clearly not the case. The GITT is easy to implement and univerally accepted as the standard for diffusivity measurement. The accuracy of D_s measurement, however, has not been reported, because there is no direct measurement method of D_s. Various methods produce different estimation results and it is not clear which method is the most accurate. This uncertainty is not desirable for such a critical parameter to cell performance. [62]. We propose that one way to quantify the error associated with GITT D_s measurement is to calculate the error between the experimental voltage data and the simulated model response. The error

$$e_{GITT} = V_{GITT} - V$$

and the RMS value

$$RMS_{GITT} = \sqrt{\sum e_{GITT}^2} \tag{1.6}$$

gives an overall metric for the accuracy of the model and D_s measurement.

The differential equation associated with the GITT model and diffusivity Eq. (1.5) is

$$\frac{dV}{d\sqrt{t}} = \frac{2V_M I_0}{SFz\sqrt{D_s\pi}} \frac{dV}{d\gamma}, \tag{1.7}$$

where S is the total specific area, F is Faraday's constant, z is the charge number of the transport species, V_M is the molar volume of the sample, and I_0 is the input current. In Eq. (1.6), $t = 0$ at the beginning of the discharge pulse. I_0 and τ are small so the slope of the OCV curve $\frac{dV}{d\gamma}$ is considered to be constant and replaced by $\frac{\Delta V_s}{\Delta\gamma}$, where

$$\Delta\gamma = \frac{I_0 \tau M_B}{z m_B F} \tag{1.8}$$

and M_B, and m_B, are the atomic and total weight of the active material, respectively.

Substitution of Eqs. (1.4) and (1.8) into Eq. (1.7) produces

$$\frac{dV}{d\sqrt{t}} = \frac{\Delta V_t}{\sqrt{\tau}}.$$

Hence, voltage response $V(t)$ in $t \in [0,\ \tau]$ is

$$V(t) = V_1 + \frac{V_2 - V_1}{\sqrt{\tau}}\sqrt{t}. \tag{1.9}$$

Thus, RMS_{GITT} can be calculated from the experimental voltage data and the four mannually selected voltages V_0, ..., V_3 using Eq. (1.9).

The problems and limitations of GITT diffusivity measurement motivate new methods that can optimally measure D_s using all of current and voltage data. The Least Squares Method (LSM) is a simple parameter estimation method for linear, time-invariant models. LSM measures the numerator and denominator polynomial coefficients of the impedance transfer function that optimally fit the current and voltage data [3, 51]. In [54], this method is successfully used to track the evolution of State-Of-Health (SOH)-related parameters, including diffusion time constant,

capacity, and ohmic resistance, through a Lithium-Ion battery's cycle life.

1.5 Overview of Present Work

In this research, Chapter 2 addresses the modeling of a VRLA battery. The Ritz method has been shown to be numerically efficient and accurate in comparison with the other techniques[26] and is therefore used to a battery model. The battery is modeled as a switched linear system[39, 40] by using different submodels for charge and discharge and determining a rule for switching between submodels. The model is then simulated and validated with experimental voltage data. After that, the low-order Ritz model is further simplified to produce a dynamic averaged model which can be realized as an equivalent circuit, providing electrochemical understanding of the equivalent circuit model in [22].

Chapter 3 provides a solution to the SOC estimation of VRLA batteries. Linear and switched linear models are developed for VRLA batteries and their voltage responses are compared with experimental results. Based on these switched linear models, we design SOC estimators by solving a convex optimization problem based on Linear Matrix Inequalities (LMIs)[69]. This produces an switched Luenberger observer which is exponentially stable. Luenberger observers are also designed from the linear models to estimate SOC. The SOC estimation prediction accuracies are compared with SOC data from experiments and the Current Integration and Voltage Lookup methods.

Chapter 4 applies the Least Squares Method (LSM) to estimate the parameters and SOH of a Valve Regulated Lead-Acid (VRLA) battery from experimental voltage and current data. The VRLA battery model is second order with four polynomial coefficients to be estimated. The reliability of the parameter estimates are evaluated with model voltage prediction error RMS.

Chapter 5 develops a Least Squares Galvanostatic Intermittent Titration Technique (LS-GITT) that uses all of the voltage data from a GITT test to optimally tune the diffusivity in a reduced order solid phase diffusion model. The accuracy of GITT and LS-GITT are calculated and compared for the NCM coin cell data in Fig. 1.2.

Finally, Chapter 6 summarizes the conclusions and contributions of this re-

search and presents some of the promising research directions in the future based on the current work.

Chapter 2

Control-Oriented Lead-Acid Battery Modeling

The first principles model [16] can accurately predict the responses of a VRLA battery to any given dynamic current input. In this chapter, we linearize and reduce this model from 3-D to 1-D in space. Model equations obtained in this chapter serve as a basis for this research and are used for SOC estimation in Chapter 3.

2.1 Linearized Electrochemical Model

The first principles model upon which this work is based [16] comprises partial differential equations describing electrochemical reactions, heat transfer, fluid flows, convection and diffusion. These equations are coupled and nonlinear so several assumptions are introduced to simplify the model: (i) the variables are considered to be evenly distributed or equal within cross-sections parallel to the current collectors; (ii) the parameters can take on different values in the positive electrode, separator, and negative electrode but are assumed to be constant within each of these domains; (iii) solid phase potential ϕ_s is considered to be equal everywhere in each electrode due to the high conductivity of solid phase material; and (iv) gassing and other side reactions are neglected.

As shown in Fig. 1.1, each cell is divided into 3 domains: the positive electrode with $x \in (0, L)$, the separator with $x \in (L_1, L_2)$ and the negative electrode with

Table 2.1. Fixed system parameters

Parameter	Description	Value
A	Cell cross-section area, cm^2	251.61
L_1	Coordinate of the boundary between positive electrode and separator, cm	0.159
L_2	Coordinate of the boundary between negative electrode and separator, cm	0.318
L	Thickness of a cell, cm	0.477
c_{ref}	Reference H^+concentration, mol/cm^3	4.9×10^{-3}
$\bar{c}$	Average concentration of H^+ at 56% SOC, mol/cm^3	3.2548×10^{-3}
R	Universal gas constant, $J \cdot mol^{-1} \cdot K^{-1}$	8.3143
F	Faraday's constant, C/mol	96485
t_+	Transference number of H^+	0.72
R_f	average contact resistance per cell, Ω	0.0352
$\overline{U}_{PbO_2}$	Setpoint open circuit potential at 56% SOC,, V	1.8813
$\widetilde{U}_{PbO_2}$	Setpoint OCV slope at 56% SOC, $V \cdot mol^{-1} cm^3$	50.7
C_{dl}	Specific capacitance for double layer effect, F/cm^2	5.0×10^{-4}

$x \in (L_2, L)$.

Electrolyte diffusion [16] is given by

$$\varepsilon \frac{\partial c}{\partial t} = D^{\text{eff}} \frac{\partial^2 c}{\partial x^2} + \frac{a_2}{2F} a j \tag{2.1}$$

where $a_2 = 3 - 2t_+$ in the positive electrode and $a_2 = 1 - 2t_+$ in the negative electrode, $c(x,t)$ is the acid concentration, and $j(x,t)$ denotes transfer current density. Note that specific area a changes with $a = a_c$ for charge reactions and $a = a_d$ for discharge reactions. All the model parameters are defined in Tabs. 2.1 and 2.2. The parameters A, L_1, L_2, and L are from the battery specifications. The parameters c_{ref}, t_+, $\overline{U}_{PbO_2}$, $\widetilde{U}_{PbO_2}$, ε, a_2, γ, i_0, α_a, and α_c are empirical values from literature [16, 18]. The parameters R, F, D^{eff}, κ^{eff}, and κ_d^{eff} are theoretical values taken from electrochemistry and physics sources [18, 1]. All of the parameters are for 25°C. The parameters $\bar{c}$, R_f, C_{dl}, a_c, a_d, and a_{dl} are tuned to fit the experimental results.

Charge conservation in the electrolyte [16] is governed by

$$\kappa^{\text{eff}} \frac{\partial^2 \phi_e}{\partial x^2} + \kappa_d^{\text{eff}} \frac{\partial^2 c}{\partial x^2} + a j + i_{dl} = 0 \tag{2.2}$$

where $\phi_e(x,t)$ is the electrolyte potential and double layer current density $i_{dl} = a_{dl} C_{dl} \frac{\partial(\phi_s - \phi_e)}{\partial t}$. Solid-phase potential $\phi_s(x,t)$ is uniform in each electrode due to assumption (iii), so $\phi_s(x,t) = \phi_{sp}(t)$ in the positive electrode and $\phi_s(x,t) =$

$\phi_{sm}(t)$ in the negative electrode.

The Butler-Volmer Equation [70] is linearized to

$$j = \frac{R_a}{a}\eta, \tag{2.3}$$

where $R_a = a \cdot i_0 \left(\frac{\bar{c}}{c_{ref}}\right)^{\gamma} \frac{(\alpha_a+\alpha_c)F}{RT}$ with $\bar{c}$ the average acid concentration in the cell and overpotential

$$\eta = \begin{cases} \phi_{sp} - \phi_e - U_{PbO_2} & '+' \, electrode \\ 0 & separator \\ \phi_{sm} - \phi_e & '-' \, electrode \end{cases}. \tag{2.4}$$

The linearized Butler-Volmer relation in Eq. (2.3) results in negligibly small error for the small overpotential η associated with small input current. Open Circuit Voltage (OCV) U_{PbO_2} is an empirically determined nonlinear function of acid concentration c given by

$$\begin{aligned} OCV =& 1.9228 + 0.0641\ln(R_m) + 0.0120\ln^2(R_m) \\ &+ 0.0060\ln^3(R_m) + 0.0012\ln^4(R_m), \end{aligned} \tag{2.5}$$

where $R_m = 1.00322c + 0.0355c^2 + 0.0022c^3 + 0.0002c^4$. Linearization of Eq. (2.5) at average acid concentration $\bar{c}$ yields the approximation

$$U_{PbO_2} = \overline{U}_{PbO_2} + \widetilde{U}_{PbO_2} c, \tag{2.6}$$

where constant coefficients $\widetilde{U}_{PbO_2} = \frac{\partial U_{PbO_2}}{\partial c}\,|_{c=\bar{c}}$ and $\overline{U}_{PbO_2} = U_{PbO_2}(\bar{c}) - \widetilde{U}_{PbO_2}\bar{c}$ with their values being presented in Tab. 2.1.

Assumption (iv) implies that input current equals the sum of main reaction current and double layer current in each electrode. In the positive electrode,

$$\int_0^{L_1} A\left[R_a(\phi_{sp} - \phi_e - U_{PbO_2}) + a_{dl}C_{dl}\frac{\partial(\phi_{sp} - \phi_e)}{\partial t}\right]dx = I(t). \tag{2.7}$$

In the negative electrode,

$$\int_{L_2}^{L_3} A\left[R_a\left(\phi_{sm}-\phi_e\right)+a_{dl}C_{dl}\frac{\partial\left(\phi_{sm}-\phi_e\right)}{\partial t}\right]dx=-I\left(t\right) \tag{2.8}$$

In Eqs. (2.7) and (2.8), the first terms in the integrals denote main reaction current density and the second terms denote double layer current density.

In addition to these differential equations, the battery model includes current collector and electrode-separator interface boundary conditions. At the current collectors ($x=0$ and $x=L$) [18],

$$\frac{\partial\phi_e}{\partial x}=0,\frac{\partial c}{\partial x}=0. \tag{2.9}$$

At the electrode-separator interfaces ($x=L_1$ and $x=L_2$) [17],

$$\begin{aligned}\left(\kappa^{\text{eff}}\frac{\partial\phi_e}{\partial x}+\kappa_d^{\text{eff}}\frac{\partial c}{\partial x}\right)\Bigg|_+&=\left(\kappa^{\text{eff}}\frac{\partial\phi_e}{\partial x}+\kappa_d^{\text{eff}}\frac{\partial c}{\partial x}\right)\Bigg|_-,\\ D^{\text{eff}}\frac{\partial c}{\partial x}\Bigg|_+&=D^{\text{eff}}\frac{\partial c}{\partial x}\Bigg|_-.\end{aligned} \tag{2.10}$$

2.2 Discretization using Ritz Method

The Ritz method generates an approximate solution to boundary value problems by using a finite set of admissible continuous functions as a basis for the $\mathbf{L^2}$ space. Many basis function choices are available, such as Fourier series, Legendre polynomials, and power series. In this dissertation, Fourier series expansions are used because they satisfy the boundary conditions at the current collectors in Eq. (2.9) and can approach the exact solution with a small number of terms.

The acid concentration distribution c is approximated by a N-th order Fourier series $c(x,t)=\sum_{m=0}^{N-1}\Psi_m\left(x\right)c_m\left(t\right)$, where the admissible function $\Psi_m\left(x\right)=\cos\left(\frac{m\pi}{L}x\right)$. Electrolyte potential is approximated by a N-1st order Fourier series $\phi_e\left(x,t\right)=\sum_{m=1}^{N-1}\Psi_m\left(x\right)\phi_m\left(t\right)$. The electrolyte potential expansion has no constant term because the average electrolyte potential across the cell is assumed to be zero. This choice of ground lowers the model order without influencing the output voltage. Eqs. (2.3) and (2.4) are plugged into Eq. (2.2) to yield the electrolyte potential

equations for the three domains

$$\begin{cases} \kappa^{\text{eff}}\frac{\partial^2\phi_e}{\partial x^2}+\kappa_d^{\text{eff}}\frac{\partial^2 c}{\partial x^2}+R_a\left(\phi_{sp}-\phi_e-U_{PbO_2}\right) \\ \\ +a_{dl}C\left(\dot{\phi}_{sp}-\dot{\phi}_e\right)=0 \quad \text{for} \;\; 0<x<L_1, \\ \\ \kappa^{\text{eff}}\frac{\partial^2\phi_e}{\partial x^2}+\kappa_d^{\text{eff}}\frac{\partial^2 c}{\partial x^2}=0 \quad \text{for} \;\; L_1<x<L_2, \\ \\ \kappa^{\text{eff}}\frac{\partial^2\phi_e}{\partial x^2}+\kappa_d^{\text{eff}}\frac{\partial^2 c}{\partial x^2}+R_a\left(\phi_{sm}-\phi_e\right) \\ \\ +a_{dl}C\left(\dot{\phi}_{sm}-\dot{\phi}_e\right)=0 \quad \text{for} \;\; L_2<x<L. \end{cases} \tag{2.11}$$

The Ritz functions are substituted into Eq. (2.11), multiplied by $\Psi_n(x)$, and integrated across the cell to produce

$$\begin{aligned} &-\int_0^L \kappa^{\text{eff}}\Psi'_n(x)\left(\sum_{m=1}^{N-1}\Psi'_m(x)\phi_m(t)\right)dx \\ &-\int_0^L \kappa_d^{\text{eff}}\Psi'_n(x)\left(\sum_{m=1}^{N-1}\Psi'_m(x)c_m(t)\right)dx \\ &+\int_0^{L_1} R_a\Psi_n(x)\left(\phi_{sp}-\sum_{m=1}^{N-1}\Psi_m(x)\phi_m(t)\right. \\ &\left.-\overline{U}_{PbO_2}-\widetilde{U}_{PbO_2}\sum_{m=0}^{N-1}\Psi_m(x)c_m(t)\right)dx \\ &+\int_0^{L_1} a_{dl}C_{dl}\Psi_n(x)\left(\dot{\phi}_{sp}-\sum_{m=1}^{N-1}\Psi_m(x)\dot{\phi}_m(t)\right)dx \\ &+\int_{L_2}^{L} R_a\Psi_n(x)\left(\phi_{sm}-\sum_{m=1}^{N-1}\Psi_m(x)\phi_m(t)\right)dx \\ &+\int_{L_2}^{L} a_{dl}C_{dl}\Psi_n(x)\left(\dot{\phi}_{sm}-\sum_{m=1}^{N-1}\Psi_m(x)\dot{\phi}_m(t)\right)dx=0, \end{aligned} \tag{2.12}$$

where integration by parts and the boundary conditions have been used. Eq. (2.12)

is converted into matrix form

$$\mathbf{M_e}\dot{\Phi}_\mathbf{e} + \mathbf{M_{es}}\dot{\mathbf{\Phi}}_\mathbf{s} = \mathbf{K_{ec}c} + \mathbf{K_e}\mathbf{\Phi_e} + \mathbf{K_{es}}\mathbf{\Phi_s} + \mathbf{B_e u}, \tag{2.13}$$

where $\mathbf{u} = \begin{bmatrix} I \\ \overline{U}_{PbO_2} \end{bmatrix}$, $\mathbf{\Phi_s} = \begin{bmatrix} \dot{\phi}_{sp}(t) \\ \dot{\phi}_{sm}(t) \end{bmatrix}$, $\mathbf{\Phi_e} = \begin{bmatrix} \dot{\phi}_1(t) \\ \vdots \\ \dot{\phi}_{N-1}(t) \end{bmatrix}$, and $\mathbf{c} = \begin{bmatrix} c_0(t) \\ \vdots \\ c_{N-1}(t) \end{bmatrix}$.

The model matrices, including those in Eq. (2.13), are provided in Appendix A.

Similarly, substitution of the Fourier series expansions into Eqs. (2.7) and (2.8), premultiplication by $\Psi_n(x)$, and integration produces

$$\mathbf{M_s}\dot{\mathbf{\Phi}}_\mathbf{s} + \mathbf{M_{se}}\dot{\mathbf{\Phi}}_\mathbf{e} = \mathbf{K_{sc}c} + \mathbf{K_{se}}\mathbf{\Phi_e} + \mathbf{K_s}\mathbf{\Phi_s} + \mathbf{B_s u}. \tag{2.14}$$

Finally, Eq. (2.1) produces the discretized electrolyte diffusion equation

$$\mathbf{M_c}\dot{\mathbf{c}} = \mathbf{K_c c} + \mathbf{K_{ce}}\mathbf{\Phi_e} + \mathbf{K_{cs}}\mathbf{\Phi_s} + \mathbf{B_c u}. \tag{2.15}$$

Combining Eqs. (2.13), (2.14) and (2.15) in a state space model,

$$\mathbf{M_1}\dot{\mathbf{x}} = \mathbf{M_2 x} + \mathbf{M_3 u}, \tag{2.16}$$

where $\mathbf{M_1} = \begin{bmatrix} \mathbf{M_c} & 0 & 0 \\ 0 & \mathbf{M_e} & \mathbf{M_{es}} \\ 0 & \mathbf{M_{se}} & \mathbf{M_s} \end{bmatrix}$, $\mathbf{M_2} = \begin{bmatrix} \mathbf{K_c} & \mathbf{K_{ce}} & \mathbf{K_{cs}} \\ \mathbf{K_{ec}} & \mathbf{K_e} & \mathbf{K_{es}} \\ \mathbf{K_{sc}} & \mathbf{K_{se}} & \mathbf{K_s} \end{bmatrix}$, $\mathbf{x} = \begin{bmatrix} \mathbf{c} \\ \mathbf{\Phi_e} \\ \mathbf{\Phi_s} \end{bmatrix}$, and $\mathbf{M_3} = \begin{bmatrix} \mathbf{B_c} \\ \mathbf{B_e} \\ \mathbf{B_s} \end{bmatrix}$. If $\mathbf{M_1}$ is invertible, which is generally true in practice at low model orders ($N < 20$), by premultiplying $\mathbf{M_1}^{-1}$, the standard state space model is obtained as

$$\dot{\mathbf{x}} = \mathbf{A_{ss}x} + \mathbf{B_{ss}u}. \tag{2.17}$$

With contact resistance R_f, the cell voltage output

$$y = V(t) = \phi_{sp} - \phi_{sm} + R_f I(t) = \mathbf{C_{ss}x} + \mathbf{D_{ss}u}, \tag{2.18}$$

where $\mathbf{C_{ss}} = [0\ 0\ \cdots\ 0\ 1\ -1]$ and $\mathbf{D_{ss}} = [R_f\ 0]$. Eqs. (2.17) and (2.18) form a linear state space system if the parameters are constant. For dynamic current inputs involving switching between charge and discharge modes, the specific area changes so a switching law $\sigma(t)$ must be established to orchestrate this mode switching. This switched linear system is given by

$$\begin{cases} \dot{\mathbf{x}} = \mathbf{A}_{\sigma(\mathbf{t})}\mathbf{x} + \mathbf{B}_{\sigma(\mathbf{t})}\mathbf{u} \\ V(t) = \mathbf{C}_{\sigma(\mathbf{t})}\mathbf{x} + \mathbf{D}_{\sigma(\mathbf{t})}\mathbf{u}, \end{cases} \tag{2.19}$$

Switching is spatially distributed throughout the electrodes and depends on the local overpotential. In this model, the switching law $\sigma(t)$ depends on the difference between the voltage $V(t)$ and $U_{PbO_2} + R_f I(t)$. $V > U_{PbO_2} + R_f I$ triggers charge mode with discharge mode otherwise. In essence, σ uses average overpotential in both electrodes to switch.

One of the main advantages of Ritz method is its fast convergence. This means that the Ritz approximation is able to quickly approach the exact solution as approximation order N increases. Figure 2.1 shows the $\mathbf{L_2}$ error for a step input relative to a 15th order Ritz approximation. By N = 10, the error is reduced to within 0.0015% of the N = 15 value.

2.3 Model Simulation and Validation

Figure 2.2 illustrates the model-predicted and experimental voltage responses to a pulse train current input for a 100 Ah VRLA-AGM battery with 6 cells in series and 8 cells in parallel. The experimental setup is described in [71]. Before the experiment, the Pb-Acid battery has been at rest for a long period of time. Therefore, the initial acid concentration can be considered to be evenly distributed across the cell, and calculated from Eq. (2.6) using the initially measured U_{PbO_2}. The initial conditions are set to be $c_0(0) = \bar{c}$ and $\phi_{sp}(0) = U_{PbO_2}$ with all other states equal to zero.

As shown in Fig. 2.2(b), the pulse train current profile consists of alternating 6.5A (0.065 C) 240s charge/discharge pulses with a 240s rest period between them. The pulse train simulates a battery-powered locomotive assembling trains in a

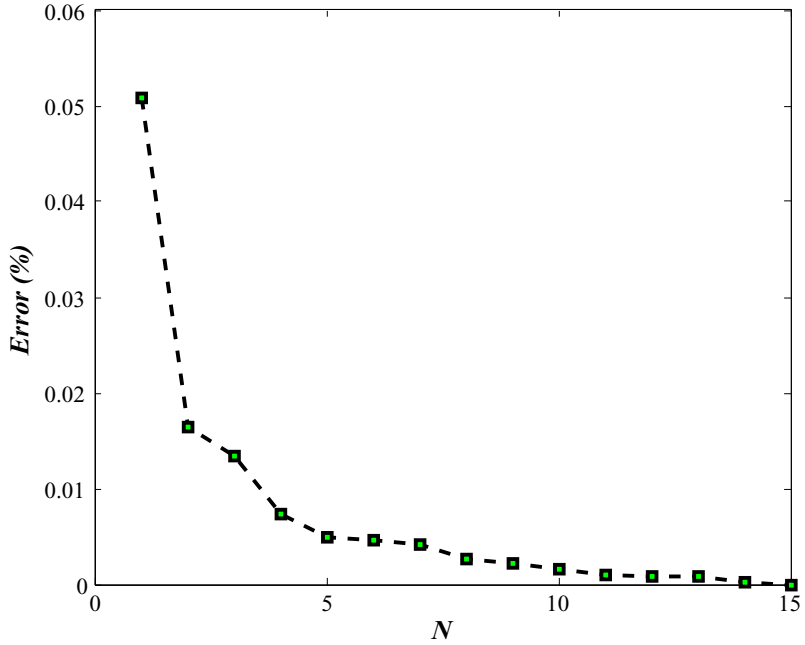

Figure 2.1. Convergence of Ritz approximation

switchyard. The battery voltage increases/decreases with charge/discharge pulses. Figure 2.2(a) demonstrates that the switched linear model (model order $N = 8$) can predict the battery output much better than charge/discharge linear models with the same order N. The charge/discharge model fails to match experimental voltage data outside of the charge/discharge periods. Hence, model switching must be taken into account when input current changes direction. Remarkably, even the simplest switched linear Ritz model ($N = 1$) shows decent agreement with the experimental voltage data, showing the fast convergence of Ritz method.

Figure 2.3 shows the spatial distributions in response to the current input in Fig. 2.2(b) with $N = 8$. These distributions start at $t = 200s$ with the battery at rest and continue every $100s$ until $t = 500s$ at the end of the first charge pulse. Figure 2.3(a) shows that the acid concentration climbs during charge period. Figure 2.3(b) reveals that electrolyte potential maintains a fairly constant distribution when the input current is constant. Figure 2.3(c) illustrates the constant distribution of solid-phase potential in each electrode.

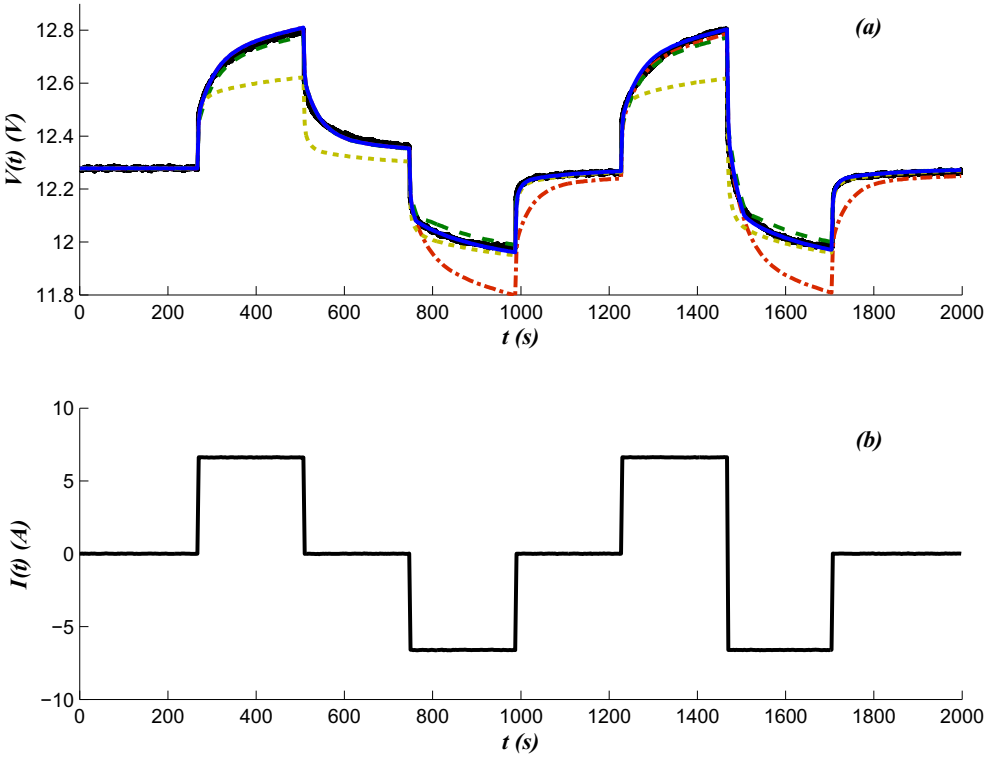

Figure 2.2. Experimental and simulated time response to a pulse charge/discharge current input: (a) Voltage output for the switched linear models with N=8 (blue-solid) and N=1 (green-dashed), charge model (red-dash-dotted), discharge model (yellow-dotted) and experiment (black-solid), (b) Input current.

2.4 Dynamic Averaged Model and Equivalent Circuit

For $N = 1$, the Ritz model has only three state variables: average concentration $\bar{c}(t)$, solid phase potentials $\phi_{sp}(t)$ and $\phi_{sm}(t)$ that are averaged in electrodes. Despite the absence of diffusion and electrolyte potential distribution, Fig. 2.2(a) shows that this low-order model maintains close with the measured voltage because critical dynamics such as the double layer effect and the Butler-Volmer equation are included. Based on these simplifications, the dynamic averaged model in state variable form is

$$\begin{cases} \dot{\mathbf{x}} = \mathbf{A}_{\mathbf{dam}}\mathbf{x} + \mathbf{B}_{\mathbf{dam}}\mathbf{u} \\ V = \mathbf{C}_{\mathbf{dam}}\mathbf{x} + \mathbf{D}_{\mathbf{dam}}\mathbf{u} \end{cases}, \tag{2.20}$$

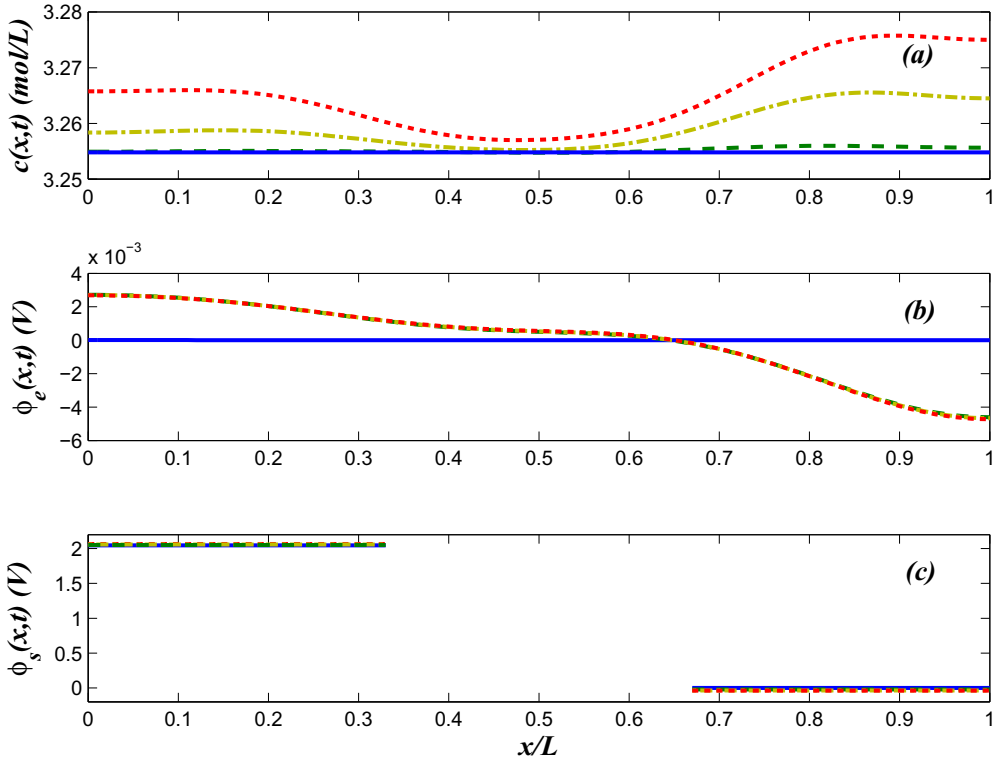

Figure 2.3. Spatial distributions in response to current input from Fig. 2.2(b) at *t=200s* (blue-solid), *300s* (green-dashed), *400s* (yellow-dash-dotted) and *500s* (red-dotted): (a) Acid concentration $c\,(x,t)$, (b) Electrolyte potential $\phi_e\,(x,t)$, and (c) Solid-phase potential $\phi_s\,(x,t)$.

where $\mathbf{A_{dam}} = \begin{bmatrix} 0 & 0 & 0 \\ \tilde{U}_{PbO_2}\lambda_2 & -\lambda_2 & 0 \\ 0 & 0 & -\lambda_4 \end{bmatrix}$, $\mathbf{B_{dam}} = \begin{bmatrix} \lambda_1 & 0 \\ \lambda_3 & \lambda_2 \\ -\lambda_5 & 0 \end{bmatrix}$, $\mathbf{C_{dam}} = \begin{bmatrix} 0 & 1 & -1 \end{bmatrix}$ and $\mathbf{D_{dam}} = \begin{bmatrix} R_f & 0 \end{bmatrix}$, with $\lambda_1 = \frac{L}{FAL[\varepsilon_1 L_1 + \varepsilon_2(L_2 - L_1) + \varepsilon_3(L - L_2)]}$, $\lambda_2 = \frac{R_{a1}}{a_{dl1}C_{dl1}}$, $\lambda_3 = \frac{1}{a_{dl1}C_{dl1}AL_1}$, $\lambda_4 = \frac{R_{a3}}{a_{dl3}C_{dl3}}$, and $\lambda_5 = \frac{1}{a_{dl3}C_{dl3}A(L-L_2)}$. The state and input vectors $\mathbf{x} = \begin{bmatrix} \mathbf{c} \\ \phi_\mathbf{e} \\ \phi_\mathbf{s} \end{bmatrix}$ and $\mathbf{u} = \begin{bmatrix} I \\ \overline{U}_{PbO_2} \end{bmatrix}$, respectively. Subscripts '1', '2', and '3' represent the positive electrode, separator, and negative electrode, respectively. This model can be realized with the equivalent circuit shown in Fig. 2.4. This equivalent circuit comprises a voltage source, three capacitors, five resistors and 4 diodes. Their values are linked to combinations of electrochemical parameters as

listed in Tab. 2.3. The charge transfer resistances R_{a1} and R_{a3} depend on specific area a with the relationship given in Eq. (2.3), which differs between charge and discharge. The diodes and resistors R_{pd}, R_{pc}, R_{md}, and R_{mc} account for this effect. The bulk capacitance is related to the battery capacity. Therefore, the gap between the equivalent circuit model and the first principles model is bridged by this low-order Ritz model.

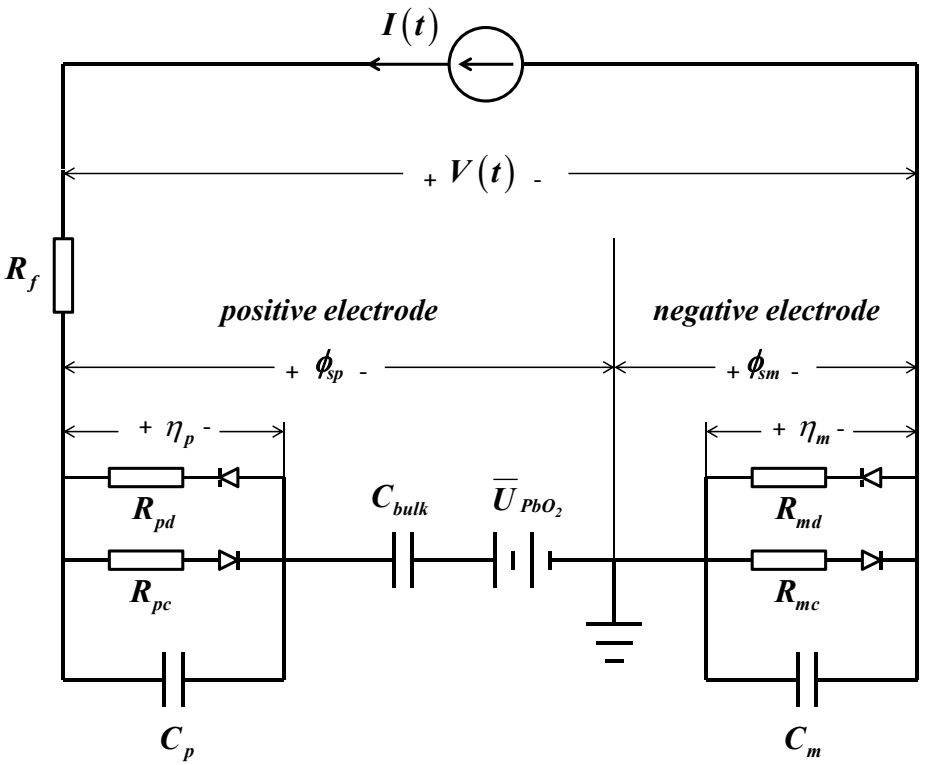

Figure 2.4. Equivalent Circuit model

Table 2.2. Spatially varying cell parameters

Parameter	Description	Positive electrode	Separator	Negative electrode
ε	Volume fraction of electrolyte	0.5818	0.8556	0.4074
D^{eff}	Diffusion coefficient, cm^2/s	1.0967×10^{-5}	1.9560×10^{-5}	6.4280×10^{-6}
a_c	Specific interfacial area during charge , cm^2/cm^3	1.277×10^5	-	1.277×10^4
a_d	Specific interfacial area during discharge, cm^2/cm^3	4.3×10^5	-	4.3×10^4
a_2	parameter associated with t_+	1.56	-	-0.44
κ^{eff}	Effective ionic conductivity of electrolyte, $\Omega^{-1}cm^{-1}$.	0.1396	0.4798	0.0447
κ_d^{eff}	Effective diffusional conductivity of electrolyte, $A \cdot cm^2/mol$	0.4817	1.6552	0.1541
γ	Exponent in Butler-Volmer Equation	0.3	-	0
i_0	Exchange current density, A/cm^2	4.45×10^{-8}	-	5.77×10^{-7}
α_a	Anodic transfer coefficient	1.15	-	1.55
α_c	Cathodic transfer coefficient	0.85	-	0.45
a_{dl}	Specific surface area for double layer effect, cm^2/cm^3	4.3×10^5		4.3×10^4

Table 2.3. Equivalent circuit components

Circuit Component	Value
R_{pc}	$\frac{1}{AL_1R_{a1c}}$
R_{pd}	$\frac{1}{AL_1R_{a1d}}$
C_p	$AL_1a_{dl1}C_{dl1}$
C_{bulk}	$\frac{FAL[\varepsilon_1L_1+\varepsilon_2(L_2-L_1)+\varepsilon_3(L-L_2)]}{\tilde{U}_{PbO_2}L}$
R_{mc}	$\frac{1}{A(L-L_2)R_{a3c}}$
R_{md}	$\frac{1}{A(L-L_2)R_{a3d}}$
C_m	$A\left(L-L_2\right)a_{dl3}C_{dl3}$

Chapter 3

State-Of-Charge Estimation

In this chapter, two switched linear models are adapted from the Ritz model in Chapter 2 and used to estimate SOC. For comparison, the switching of model parameters is ignored to develop the other three linear models. Based on these models, switched observers and Luenberger observers are designed with guranteed exponential stability using pole placement and a LMI-based convex optimization design technique. SOC estimation accuracy of these model-based methods are compared with SOC data from experiments and the Current Integration and Voltage Lookup methods.

3.1 Models and Switching Law Design for SOC Estimation

In the Ritz model given by Eq. (2.19), the input $\mathbf{u} = \begin{bmatrix} I(t) \\ \bar{U}_{\mathbf{PbO_2}} \end{bmatrix}$, state vector $\mathbf{x} = \begin{bmatrix} \mathbf{c}(t) \\ \phi_{\mathbf{e}}(t) \\ \phi_{\mathbf{s}}(t) \end{bmatrix}$, and $V(t)$ is the voltage output. The state vector elements $\mathbf{c}$, $\phi_{\mathbf{e}}$, and ϕ_s are the Fourier series coefficients of the distributions $c(x,t)$, $\phi_e(x,t)$ and $\phi_s(x,t)$. The average acid concentration $\bar{c}$, from which SOC can be calculated, is the first entry of $\mathbf{x}$ and $\mathbf{c}$. The specific area changes from charge to discharge, causing the matrices $\mathbf{A}_{\sigma(\mathbf{t})}$ and $\mathbf{B}_{\sigma(\mathbf{t})}$ to change. If the switching law

Table 3.1. Lead-Acid battery models

Model	Description
1	$\sum(\mathbf{A}_1, \mathbf{B}_1, \mathbf{C}_1, \mathbf{D}_1)$: Linear state space model based on charge parameters.
2	$\sum(\mathbf{A}_2, \mathbf{B}_2, \mathbf{C}_2, \mathbf{D}_2)$: Linear state space model based on discharge parameters.
3	$\sum_{\sigma_{sign}}(\mathbf{A_{ritz}}, \mathbf{B_{ritz}}, \mathbf{C_{ritz}}, \mathbf{D_{ritz}})_M$: Switched linear model with switching law σ_{sign}.
4	$\sum_{\sigma_{lp}}(\mathbf{A_{ritz}}, \mathbf{B_{ritz}}, \mathbf{C_{ritz}}, \mathbf{D_{ritz}})_M$: Switched linear model with switching law σ_{lp}.
5	$\sum(A_{avg}, \mathbf{B_{avg}}, C_{avg}, \mathbf{D_{avg}})$: Averaged model.

depends only on the input or time then the system is a switched linear system symbolized as $\sum_{\sigma}(\mathbf{A_{ritz}}, \mathbf{B_{ritz}}, \mathbf{C_{ritz}}, \mathbf{D_{ritz}})_M$, where $\sigma(t)$ is the switching law and $M = 2$ is the number of subsystems. The charge and discharge subsystems of $\sum_{\sigma}(\mathbf{A_{ritz}}, \mathbf{B_{ritz}}, \mathbf{C_{ritz}}, \mathbf{D_{ritz}})_M$ are $\sum(\mathbf{A}_1, \mathbf{B}_1, \mathbf{C}_1, \mathbf{D}_1)$ and $\sum(\mathbf{A}_2, \mathbf{B}_2, \mathbf{C}_2, \mathbf{D}_2)$, respectively.

In this chapter, we use fifth-order Ritz model (N = 2) summarized in Tab. 3.2. The switched linear model in Eq. (2.19) approximates the more complex and nonlinear switching that is distributed throughout the electrodes and depends on the local overpotential. In this chapter, the switching law σ is approximated as a function solely of input current $I(t)$. Two switching laws are investigated that approximate the delay between current and overpotential switching.

The first switching law σ_{sign} is

$$i = \begin{cases} 1 & I(t) \geq \epsilon_s \\ 2 & I(t) \leq -\epsilon_s \end{cases}, \tag{3.1}$$

where the deadband ϵ_s is adjusted to more closely match the full model. Inside the deadband ($-\epsilon_s < I < \epsilon_s$), the model maintains the charge or discharge mode with which it entered. The second switching law σ_{lp} includes a first-order low-pass filter with a time constant τ that can be tuned to match the full model,

$$\frac{I_f(s)}{I(s)} = \frac{1}{\tau s + 1}.$$

The switching law σ_{lp} depends on the filter output,

$$i = \begin{cases} 1 & I_f(t) \geq 0 \\ 2 & I_f(t) < 0 \end{cases}. \tag{3.2}$$

The simplest battery model assumes that the output voltage solely depends on averaged acid concentration

$$\begin{cases} \dot{\bar{c}} = A_{avg}\bar{c} + \mathbf{B_{avg}}\mathbf{u} \\ V(t) = C_{avg}\bar{c} + \mathbf{D_{avg}}\mathbf{u}, \end{cases} \tag{3.3}$$

where $A_{avg} = 0$, $\mathbf{B_{avg}} = \begin{bmatrix} \frac{3}{FAL(\varepsilon_1+\varepsilon_2+\varepsilon_3)} & 0 \end{bmatrix}$, $C_{avg} = \widetilde{U}_{\mathbf{PbO_2}}$, and $\mathbf{D_{avg}} = \begin{bmatrix} 0 & 1 \end{bmatrix}$. Tables 2.1 and 2.2 list all of the parameters used in the five models summarized in Tab. 3.1. All of the models include average concentration $\bar{c}(t)$ in their state vectors. SOC is linearly related to $\bar{c}$ by

$$SOC = (240.1579\bar{c} - 0.2254) \times 100\% \tag{3.4}$$

for $10\% < SOC < 90\%$ at 25°C [38]. Thus, all of the models can predict SOC.

3.2 Experimental Results

Figure 3.1 shows the model-predicted and experimental voltage responses to a pulse current input for a 100 Ah 12V AGM VRLA battery. The current input (Fig.3.1(c)) consists of two, 240s, 6.5A (0.065C) charge/discharge pulses with 240s rest periods in between. An AE Techron LVC 5050 linear amplifier controlled by dSPACE produces the current input. Note that the experiments are performed at 25°C. The experimental voltage response (black-solid curve in Fig.3.1(a) and (b)) starts at 12.3V (55.6% SOC) after a long rest period and increases/decreases with charge/discharge pulses. The switched linear models in Fig.3.1(a) clearly outperform the other models shown in Fig.3.1(b). The switched linear model-predicted voltage closely matches the experiment results. The linear models match the corresponding charge or discharge curves but not both, well-motivating a switched

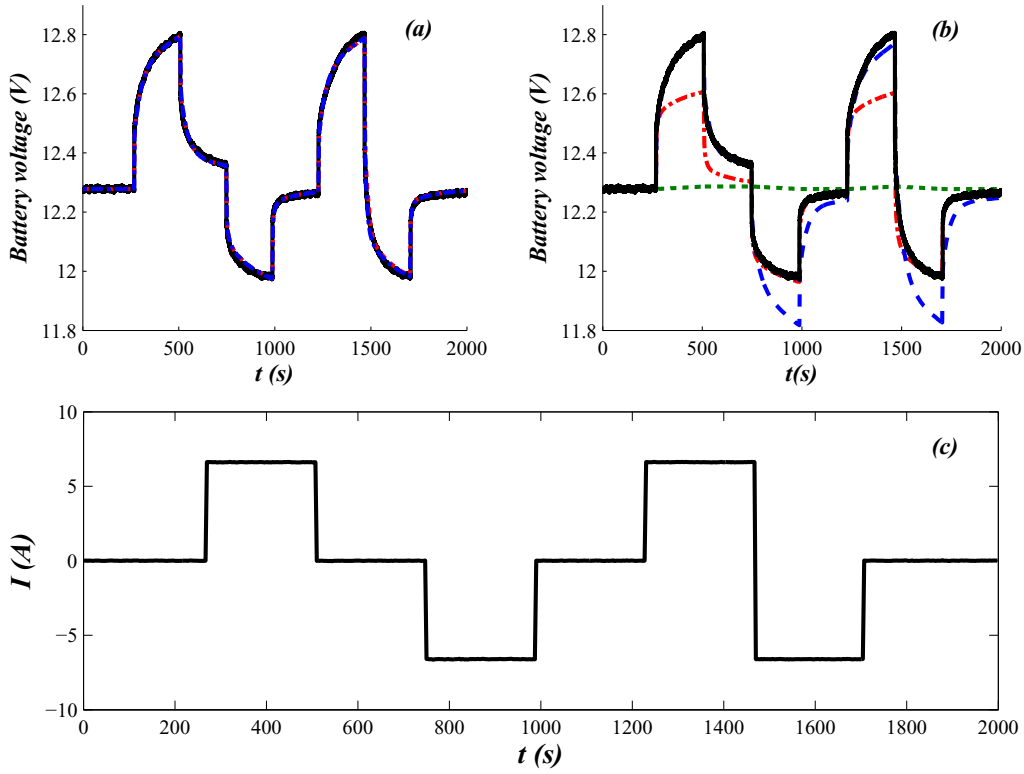

Figure 3.1. Battery voltage response: (a) Models 3 (blue-dash-dotted) and 4 (red-dashed) and experiment (black-solid), (b) Models 1 (blue-dashed), 2 (red-dash-dotted), and 5 (green-dotted), and experiment (black-solid), (c) Current applied to the battery.

linear approach. The averaged model does a poor job of tracking voltage swings.

3.2.1 State Observer Design

The accuracy of the switched linear models motivates the development of a switched Luenberger SOC estimator. A schematic diagram of a switched Luenberger observer [41] is shown in Fig. 3.2, where the battery model defined by Eq.(2.19) is used and $\sigma(t)$ can be either the deadband (Model 3) or low-pass filter (Model 4) switching laws. The switched Luenberger observer is

$$\begin{cases} \dot{\hat{\mathbf{x}}} = \mathbf{A}_{\sigma(\mathbf{t})}\hat{\mathbf{x}} + \mathbf{B}_{\sigma(\mathbf{t})}\mathbf{u} + \mathbf{L}_{\sigma(\mathbf{t})}\left(\hat{V}(t) - V(t)\right) \\ \hat{V}(t) = \mathbf{C}_{\sigma(\mathbf{t})}\hat{\mathbf{x}} + \mathbf{D}_{\sigma(\mathbf{t})}\mathbf{u}, \end{cases} \tag{3.5}$$

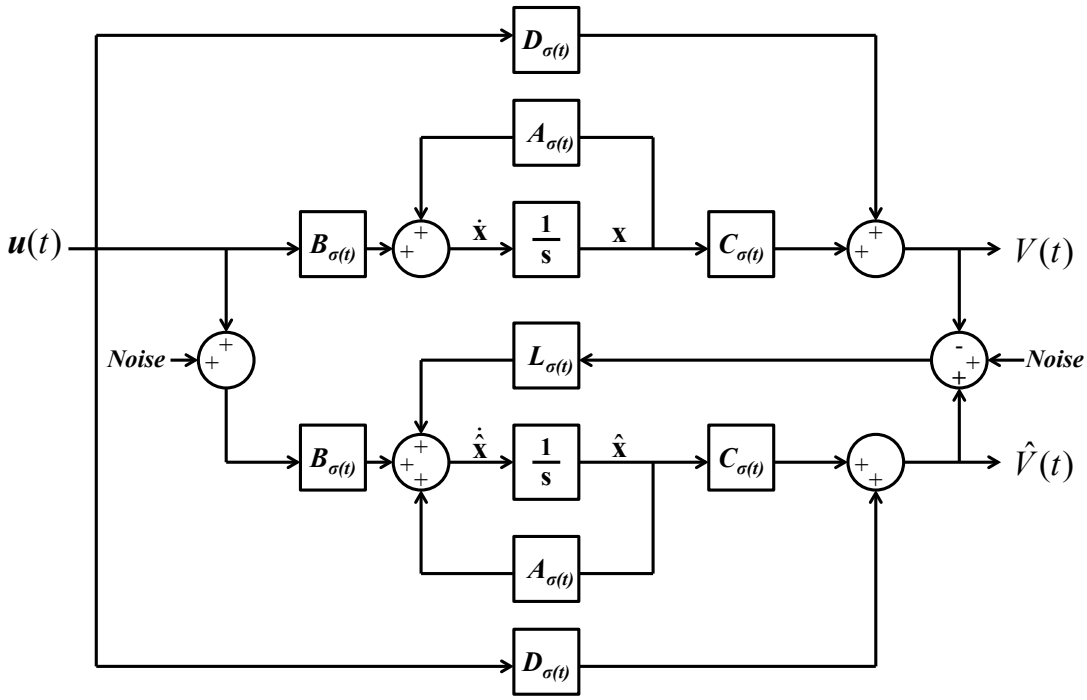

Figure 3.2. Switched Luenberger observer diagram

where the gain matrix $\mathbf{L}_{\sigma(\mathbf{t})}$ is designed to ensure that $\hat{\mathbf{x}}(t) \to \mathbf{x}(t)$ as $t \to \infty$.

From Eqs. (2.19) and (3.5), the error $\mathbf{e} = \hat{\mathbf{x}} - \mathbf{x}$ has switched linear dynamics

$$\dot{\mathbf{e}} = \left(\mathbf{A}_{\sigma(\mathbf{t})} - \mathbf{L}_{\sigma(\mathbf{t})}\mathbf{C}_{\sigma(\mathbf{t})}\right)\mathbf{e}. \tag{3.6}$$

If there exists a Common Quadratic Lyapunov Function (CQLF) $\mathbf{e}^T\mathbf{P}\mathbf{e}$ for all of the error dynamics subsystems given in Eq. (3.6), then the error dynamics is asymptotically stable. A CQLF exists if and only if there exists a $\mathbf{P} > 0$, such that for every subsystem $i \in M = \{1, 2\}$,

$$\left(\mathbf{A}_i - \mathbf{L}_i\mathbf{C}_i\right)^T\mathbf{P} + \mathbf{P}\left(\mathbf{A}_i - \mathbf{L}_i\mathbf{C}_i\right) < \mathbf{0}. \tag{3.7}$$

For the third-order Ritz model (N = 1) given by Eq. (2.20), Appendix B shows a direct Switched Luenberger Observer design method that guarantees the existence of solutions $\mathbf{P}$, $\mathbf{L}_1$, and $\mathbf{L}_2$ to Eq. (3.7) and a CQLF. For higher order Ritz models, there is no strict proof of the existence of CQLF, however, there are infinitely many selections of $\mathbf{P}$ and gains $\mathbf{L}_1$ and $\mathbf{L}_2$ that solve Eq. (3.7) in most

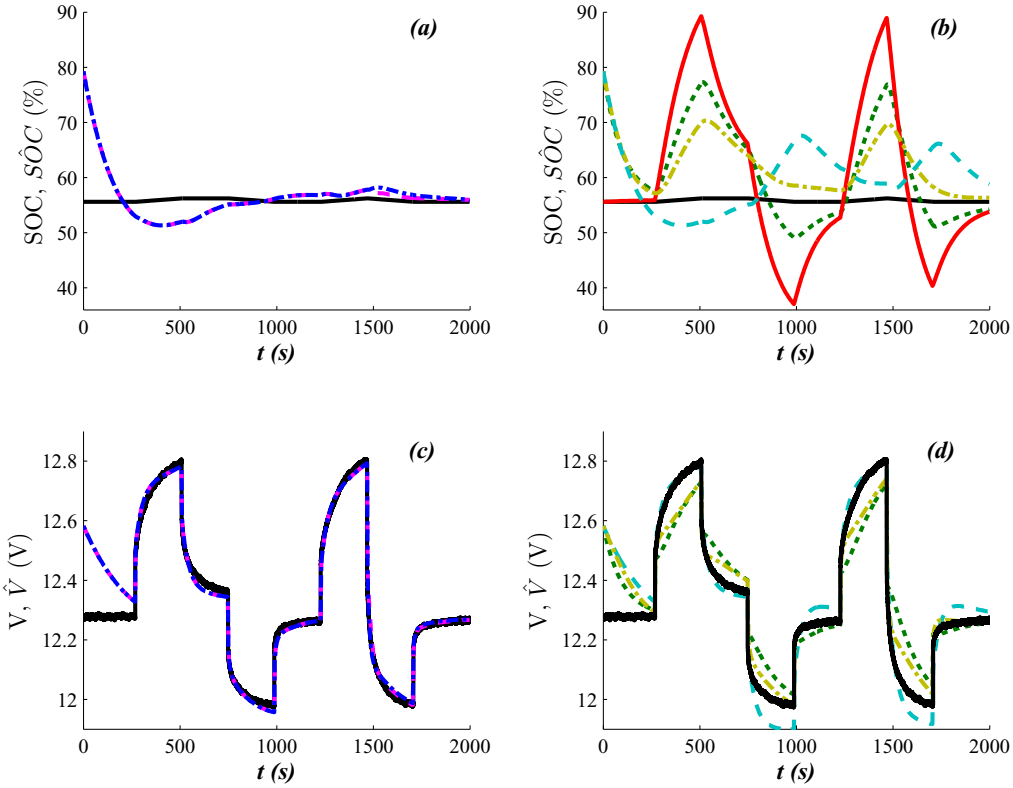

Figure 3.3. SOC estimation results: (a) Estimated SOC based on switched linear models 3 (blue-dash-dotted) and 4 (pink-dashed) and experimentally calculated SOC (black-solid), (b) Estimated SOC based on linear models 1 (cyan-dashed), 2 (yellow-dash-dotted), and 5 (green-dotted), Voltage Lookup Method (red-solid), and experimental data (black-solid), (c) Estimated voltage based on switched linear models 3 (blue-dash-dotted) and 4 (pink-dashed) and measured voltage (black-solid), (d) Estimated voltage based on linear models 1 (cyan-dashed), 2 (yellow-dash-dotted), and 5 (green-dotted) and measured voltage (black-solid).

cases. By minimizing a cost function, an appropriate choice of $\mathbf{P}$ and gains $\mathbf{L}_1$ and $\mathbf{L}_2$ can be obtained. Previous researchers have proposed many optimization methods to stabilize a switched linear system [72, 73]. However, the cost functions in these methods often lead to a fast error convergence. For the sluggish dynamics in the VRLA battery, such methods tend to produce very high gains $\mathbf{L}_1$ and $\mathbf{L}_2$, making the designed observer vulnerable to noise and causing numerical issues. To tackle this problem, we can add a weighting matrix $\mathbf{R}$ to penalize the gain $\mathbf{L}_i$. Inspired by a LMI-based LQR control problem in [74], we construct the following

optimization problem to design a stable estimator:

$$\begin{aligned} &\min_{(\mathbf{L}_i,\mathbf{P})} \left\{ \mathrm{tr}\left(\mathbf{QP}\right) + \max_{i\in M} \left\{ \mathrm{tr}\left(\mathbf{L}_i\mathbf{R}\mathbf{L}_i^T\mathbf{P}\right)\right\}\right\} \\ &\text{subject to} \qquad \mathbf{P} > \mathbf{0}, \qquad \forall\, i \in M = \{1,\ 2\}\,, \\ &\left(\mathbf{A}_i - \mathbf{L}_i\mathbf{C}_i\right)^T\mathbf{P} + \mathbf{P}\left(\mathbf{A}_i - \mathbf{L}_i\mathbf{C}_i\right) < \mathbf{0}. \end{aligned} \tag{3.8}$$

Let $\mathbf{L}_i = \mathbf{P}^{-1}\mathbf{M}_i^T$. The quadratic term

$$\begin{aligned} \max_{i\in M}\left\{\mathrm{tr}\left(\mathbf{L}_i\mathbf{R}\mathbf{L}_i^T\mathbf{P}\right)\right\} &= \max_{i\in M}\left\{\mathrm{tr}\left(\mathbf{R}^{1/2}\mathbf{L}_i^T\mathbf{P}\mathbf{L}_i\left(\mathbf{R}^{1/2}\right)^T\right)\right\} \\ &= \max_{i\in M}\left\{\mathrm{tr}\left(\mathbf{R}^{1/2}\mathbf{M}_i\mathbf{P}^{-1}\mathbf{M}_i^T\left(\mathbf{R}^{1/2}\right)^T\right)\right\}. \end{aligned} \tag{3.9}$$

Then we can redesign a similar optimization problem as

$$\begin{aligned} &\min_{(\mathbf{M_i},\mathbf{P},\hat{\mathbf{X}})} \mathrm{tr}\left(\mathbf{QP}\right) + \mathrm{tr}\left(\hat{\mathbf{X}}\right) \\ &\text{subject to } \hat{\mathbf{X}} > \mathbf{R}^{1/2}\mathbf{M}_i\mathbf{P}^{-1}\mathbf{M}_i^T\left(\mathbf{R}^{1/2}\right)^T,\ \forall\, i \in M \\ &\mathbf{A}_i^T\mathbf{P} + \mathbf{P}\mathbf{A}_i - \mathbf{C}_i^T\mathbf{M}_i - \mathbf{M}_i^T\mathbf{C}_i < \mathbf{0},\ \mathbf{P} > \mathbf{0}. \end{aligned} \tag{3.10}$$

By Schur Complement [75], Eq. (3.10) is converted into the LMI-based optimization problem as follows:

$$\begin{aligned} &\min_{(\mathbf{M}_i,\mathbf{P},\hat{\mathbf{X}})} \mathrm{tr}\left(\mathbf{QP} + \hat{\mathbf{X}}\right), \\ &\text{subject to} \quad \begin{bmatrix} \hat{\mathbf{X}} & \mathbf{R^{1/2}M}_i \\ \mathbf{M}_i^T\mathbf{R^{1/2}}^T & \mathbf{P} \end{bmatrix} > \mathbf{0}, \qquad \forall\, i \in M, \\ &\mathbf{A}_i^T\mathbf{P} + \mathbf{P}\mathbf{A}_i - \mathbf{C}_i^T\mathbf{M}_i - \mathbf{M}_i^T\mathbf{C}_i < \mathbf{0},\ \mathbf{P} > \mathbf{0}, \end{aligned} \tag{3.11}$$

where $\mathbf{M}_i \in \mathbb{R}^{p\times n}$, $\mathbf{Y} \in \mathbb{R}^{n\times n}$, and $\hat{\mathbf{X}} \in \mathbb{R}^{p\times p}$ are matrix variables with n being the number of state variables and p the number of outputs in Eq. (2.19). Eq. (3.11) searches for the 'optimal' selection out of all the possible combinations of gains $\mathbf{L}_i$ and $\mathbf{P} > \mathbf{0}$ such that a CQLF exists. The solution is feasible as long as the CQLF existence criterion in Eq. (3.7) is met. This approach yields observer feedback gain $\mathbf{L}_i = \mathbf{P}^{-1}\mathbf{M}_i^T$ for subsystem i and CQLF $\mathbf{e}^T\mathbf{P}\mathbf{e}$ exists for all of the error dynamics

subsystems given in Eq. (3.6), ensuring exponential stability of the observer. A short proof of the exponential stability is provided as follows:

The CQLF $V = \mathbf{e}^T\mathbf{P}\mathbf{e} > 0, \ \forall\, \mathbf{e} \neq \mathbf{0}$, is radially unbounded and decresent. Let $\mathbf{S}_i = (\mathbf{A}_i - \mathbf{L}_i\mathbf{C}_i)^T \mathbf{P} + \mathbf{P}(\mathbf{A}_i - \mathbf{L}_i\mathbf{C}_i)$, then

$$\dot{V} = \begin{cases} -\mathbf{e}^T\mathbf{S}_1\mathbf{e} & \sum(\mathbf{A}_1, \mathbf{B}_1, \mathbf{C}_1, \mathbf{D}_1) \text{ is active} \\ -\mathbf{e}^T\mathbf{S}_2\mathbf{e} & \sum(\mathbf{A}_2, \mathbf{B}_2, \mathbf{C}_2, \mathbf{D}_2) \text{ is active} \end{cases}.$$

So $\dot{V} \leq -\min\{\lambda_{min}(\mathbf{S}_1), \lambda_{min}(\mathbf{S}_2)\} \|\mathbf{e}\|_2 \leq -\lambda V$, where

$$\lambda = -\min\{\lambda_{min}(\mathbf{S}_1), \lambda_{min}(\mathbf{S}_2)\} / \lambda_{max}(\mathbf{P}).$$

Hence, the error dynamics is exponentially stable.

The switching laws σ_{sign} and σ_{lp} are based on $I(t)$, which is known, hence $\hat{\mathbf{x}}(t) \to \mathbf{x}(t)$ as $t \to \infty$ for both switching laws. The switched linear models 3 and 4 have 5 state variables so we choose weighting matrices

$$\mathbf{Q} = \begin{bmatrix} 0.006 & 0 & 0 & 0 & 0 \\ 0 & 0.008 & 0 & 0 & 0 \\ 0 & 0 & 0.008 & 0 & 0 \\ 0 & 0 & 0 & 0.008 & 0 \\ 0 & 0 & 0 & 0 & 0.008 \end{bmatrix}$$

and $\mathbf{R} = 100000$. Note that we use a large $\mathbf{R}$ compared with $\mathbf{Q}$ to avoid excessively fast error convergence so that mild observer gains are obtained. For models 1 and 2, the constant observer gain matrix $\mathbf{L}_i$ is the same as the corresponding observer gain matrix in the switched design. Another Luenberger observer is designed based on first-order linear model 5 by moving the one pole at origin to $s = -0.01$.

Figure 3.3 shows the SOC estimation results for the input current in Fig. 3.1 (c). The initial SOC is determined to be 55.6% by measuring the Open Circuit Voltage and using an empirical relationship with the average acid concentration $\bar{c}$ (or SOC) at room temperature. The experimental SOC is determined using the Current Counting Method based on this known $SOC(0)$. For the SOC estimators, however, the $SOC(0)$ is initiated at 79%. Figures 3.3 (a) and (c) show the results for the switched linear observers. The voltage and SOC estimates converge to near

their actual values in 300s and 650s, respectively. The linear and averaged model-based estimators shown in Figs. 3.3 (b) and (d) have much poorer performance, showing large SOC and voltage errors throughout the test. Voltage lookup also shows poor SOC estimation.

3.2.2 SOC Estimation Results

To provide quantitative evaluation of estimation performance, the $\mathbf{L_2}$ and $\mathbf{L}_\infty$ error norms are calculated. The $\mathbf{L_2}$ norm is

$$\| e_{SOC}(t) \|_2 = \sqrt{\frac{1}{N_s}\left(\sum_{n=1}^{N_s}\left|e_{SOC}\left(\frac{n}{f_s}\right)\right|^2\right)} \tag{3.12}$$

and the $\mathbf{L}_\infty$ norm is

$$\| e_{SOC}(t) \|_\infty = \max_{n\in(1,N_s)}\left|e_{SOC}\left(\frac{n}{f_s}\right)\right|, \tag{3.13}$$

where $e_{SOC}(t) = \hat{SOC} - SOC$, the sampling rate $f_s = \frac{1}{3}Hz$, and the number of samples $N_s = 668$. The SOC estimators are initialized with $\hat{SOC}(0) = SOC(0)$ and simulated for 2000s. Table 3.3 shows that estimators based on model 3 and 4 have the least SOC estimation error, with σ_{lp} slightly outperforming σ_{sign}. This confirms that the additional complexity of the switched linear design and the additional computation required by the low pass filter may be warranted in some applications. The high errors (20 - 40%) of the Voltage Lookup method would be unacceptable in most applications. If a longer transient time is acceptable then the Voltage Lookup method error can be reduced by increasing the filter time constant to sharply reduce the higher frequency error spikes. The 5% - 10% errors associated with the linear model-based observers may be a worthwhile tradeoff relative to the switched linear designs due to their simple and computationally less demanding implementation. The performance of the average model-based observer lies between the linear observers and Voltage Lookup method. This observer has large error spikes at the start and end of pulses. Figure 3.4 shows the simulated results for the aggressive current input (Fig. 3.4(c)). The σ_{lp}-based outperforms the σ_{sign}-based observer in this case as well. The σ_{lp}-based estimator does a better

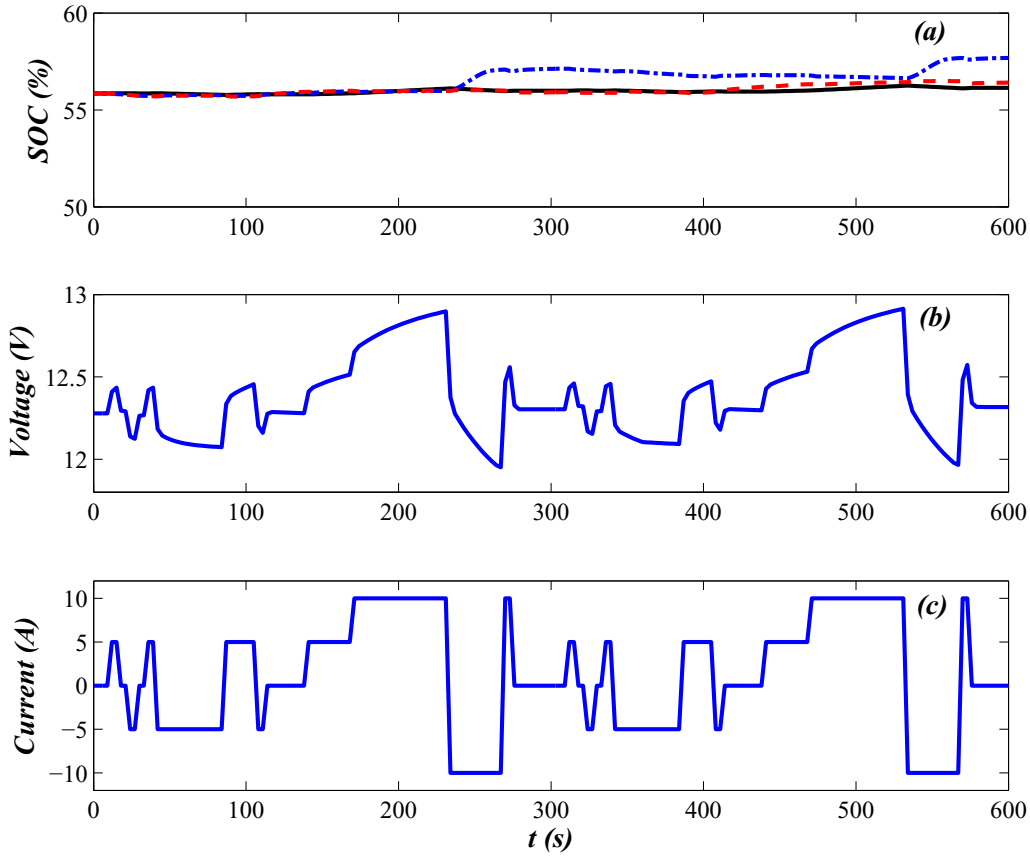

Figure 3.4. SOC estimation results: (a) SOC estimators based on model 3 (blue-dash-dotted) and 4 (red-dashed) and calculated SOC (black-solid), (b) Simulated battery voltage, and (c) Simulated current.

job of approximating the actual cell dynamics.

In Figs. 3.3 and 3.4 the SOC stayed near 55.6% and did not test the assumption of small SOC variation. Figure 3.5 shows the results for another experiment where the battery is deeply discharged at 6.5A (0.065C) from $SOC \approx 70\%$ to 40%. The current does not change sign during the experiment so observers based on models 2 - 4 produce the same results, shown as the yellow-dashed line in Fig. 3.5(a). Although the estimated SOC is more accurate than that produced by the average model-based observer, it only matches the actual value near the linearization point of 55.6% SOC. This is primarily due to the fact that the battery parameters depend on SOC. In addition, temperature changes influence the battery parameters through, for example, the Arrhenius Equation [76]. The OCV changes with tem-

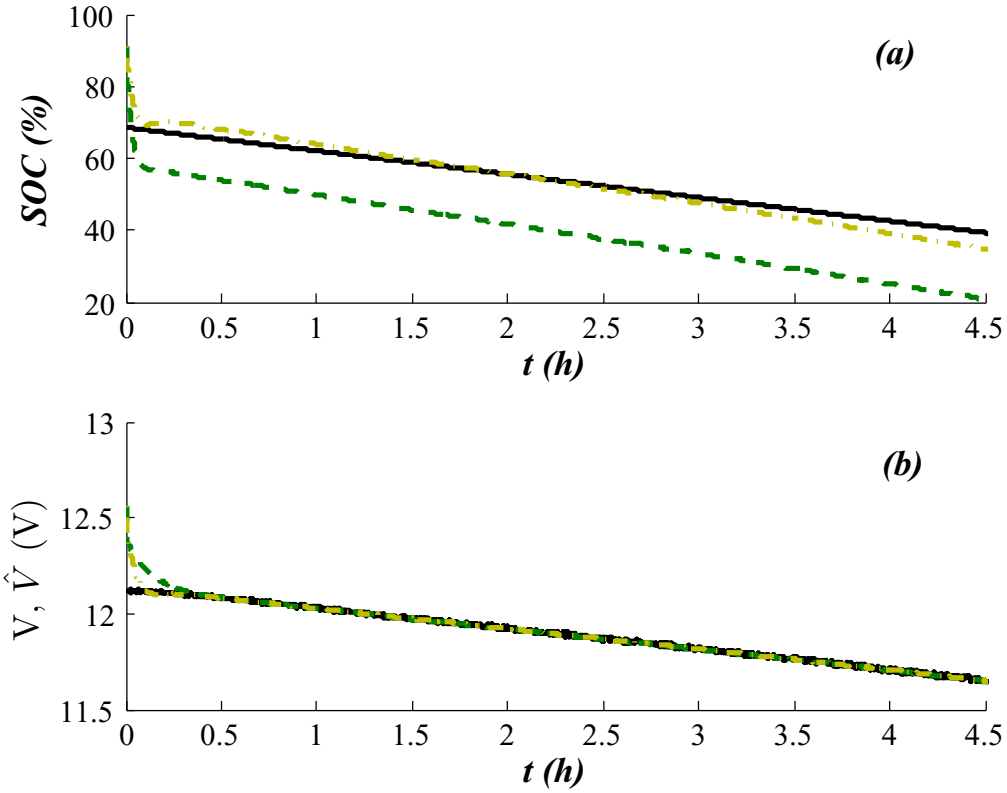

Figure 3.5. SOC estimation during 0.065C discharge from 70% to 40% SOC: (a) Actual SOC (black-solid) and SOC estimation based on the model 2 (yellow-dash-dotted) and averaged model (green-dashed) (b) Voltage tracking to experimental voltage data (black-solid) of SOC estimators based on the model 2 (yellow-dash-dotted) and averaged model (green-dashed).

perature at about $0.02V/°\text{C}$ [1]. These effects can be compensated for by using a gain scheduling method, where the SOC estimator parameters and gains change with SOC and temperature. Although stability is difficult to prove, a gain scheduling design would be practically stable because the SOC and temperature change very slowly (often $> 1 - 10$ hr) compared to the time constant of the estimators (about 5 min).

Table 3.2. Fifth-order Ritz model state matrices

Matrix	Value*
M_T	$\begin{bmatrix} 0.1590\,(\varepsilon_1+\varepsilon_2+\varepsilon_3) & 0.1315\,(\varepsilon_1-\varepsilon_3) & 0 & 0 & 0 \\ 0.1315\,(\varepsilon_1-\varepsilon_3) & 0.1124\,(\varepsilon_1+\varepsilon_3)+0.0138\varepsilon_2 & 0 & 0 & 0 \\ 0 & 0 & 0.1124\,(a_{dl1}C_{dl1}+a_{dl3}C_{dl3}) & -0.1315a_{dl1}C_{dl1} & 0.1315a_{dl3}C_{dl3} \\ 0 & 0 & 0.1315a_{dl1}C_{dl1} & -a_{dl1}C_{dl1}L_1 & 0 \\ 0 & 0 & -0.1315a_{dl3}C_{dl3} & 0 & -a_{dl3}C_{dl3}\,(L-L_2) \end{bmatrix}$
M_A	$\begin{bmatrix} -0.1590\frac{\widetilde{U}_{PbO_2}a_{21}R_{a1}}{2F} & -0.1315\frac{\widetilde{U}_{PbO_2}a_{21}R_{a1}}{2F} & -0.1315\left(\frac{a_{21}R_{a1}}{2F}-\frac{a_{23}R_{a3}}{2F}\right) & 0.1590\frac{a_{21}R_{a1}}{2F} & 0.1590\frac{a_{23}R_{a3}}{2F} \\ -0.1315\frac{\widetilde{U}_{PbO_2}a_{21}R_{a1}}{2F} & -2.0226\left(D_1^{\mathrm{eff}}+D_3^{\mathrm{eff}}\right)-6.3004D_2^{\mathrm{eff}}-0.1124\frac{\widetilde{U}_{PbO_2}a_{21}R_{a1}}{2F} & -0.1124\left(\frac{a_{21}R_{a1}}{2F}+\frac{a_{23}R_{a3}}{2F}\right) & 0.1315\frac{a_{21}R_{a1}}{2F} & -0.1315\frac{a_{23}R_{a3}}{2F} \\ -0.1315\widetilde{U}_{PbO_2}R_{a1} & -2.0226\left(\kappa_{d1}^{\mathrm{eff}}+\kappa_{d3}^{\mathrm{eff}}\right)-6.3004\kappa_{d2}^{\mathrm{eff}}-0.1124\widetilde{U}_{PbO_2}R_{a1} & -2.0226\left(\kappa_1^{\mathrm{eff}}+\kappa_3^{\mathrm{eff}}\right)-6.3004\kappa_2^{\mathrm{eff}}-0.1124\,(R_{a1}+R_{a3}) & 0.1315R_{a1} & -0.1315R_{a3} \\ -0.1590\widetilde{U}_{PbO_2}R_{a1} & -0.1315\widetilde{U}_{PbO_2}R_{a3} & -0.1315R_{a1} & R_{a1}L_1 & 0 \\ 0 & 0 & 0.1315R_{a3} & 0 & R_{a3}\,(L-L_2) \end{bmatrix}$
M_B	$\begin{bmatrix} 0 & -0.1590\frac{a_{21}R_{a1}}{2F} \\ 0 & -0.1315\frac{a_{21}R_{a1}}{2F} \\ 0 & -0.1315R_{a1} \\ -\frac{1}{A} & -R_{a1}L_1 \\ \frac{1}{A} & 0 \end{bmatrix}$
$\mathbf{A_{ritz}}$	$\mathbf{M}_T^{-1}\mathbf{M}_A$
$\mathbf{B_{ritz}}$	$\mathbf{M}_T^{-1}\mathbf{M}_B$
$\mathbf{C_{ritz}}$	$\begin{bmatrix} 0 & 0 & 0 & 1 & -1 \end{bmatrix}$
$\mathbf{D_{ritz}}$	$\begin{bmatrix} R_{ct} & 0 \end{bmatrix}$

*subscripts 1, 2, and 3 denote the spatially varying system parameters in the positive electrode, seperator, and negative electrode, respectively. *i.e,* D_1^{eff} denotes the value of D^{eff} in the positive electrode.

Table 3.3. SOC estimation error

Method	$\mathbf{L_2}$ Error	$\mathbf{L_\infty}$ Error
Model 4	0.20%	0.53%
Model 3	0.35%	1.12%
Model 1	4.93%	11.43%
Model 2	5.04%	10.12%
Model 5	10.00%	23.68%
Voltage Lookup	19.41%	40.20%

Chapter 4

State-Of-Health Estimation

In this chapter, the third order dynamic averaged model developed in Chapter 2 is further simplified by combining the positive and negative electrode to generate a second order impedance transfer function model. The four polynomial coefficients of the transfer function are explicitly correlated to the ohmic resistance, cell capacity, and double layer time constant, providing an excellent model for SOH estimation. We apply the Least Squares Method (LSM) to estimate these SOH-related parameters and evaluate the estimation error with model voltage prediction error RMS, providing three possible SOH/SOP estimation methods.

4.1 Model Development for SOH Estimation

The dynamic averaged model developed in Chapter 2 is a third-order model for VRLA batteries. In this research, we increase identifiability by reducing the model to second order by combining the positive and negative electrodes. We also assume unidirectional current flow to eliminate switched nonlinearity. The resulting transfer function is

$$\frac{V(s)}{I(s)} = \frac{b_2 s^2 + b_1 s + b_0}{s^2 + a_1 s} = R_f + \frac{\widetilde{U}_{PbO_2}\Delta c}{Qs} + \frac{R_c}{\tau_{dl} s + 1}, \tag{4.1}$$

where $b_2 = R_f$, $b_1 = \frac{R_f + R_c}{\tau_{dl}} + \frac{\widetilde{U}_{PbO_2}\Delta c}{Q}$, $b_0 = \frac{\widetilde{U}_{PbO_2}\Delta c}{\tau_{dl} Q}$, $a_1 = \frac{1}{\tau_{dl}}$, R_f is the ohmic resistance, $R_c = \frac{RT}{A\delta_1 a_c i_0 (\alpha_a + \alpha_c) F} \left(\frac{c_{ref}}{\bar{c}}\right)^{\gamma}$ is the charge transfer resistance, $\widetilde{U}_{PbO_2}$ is the slope of the open circuit potential curve, Δc is the acid concentration change

Table 4.1. Dynamic Averaged Model Parameters

Parameter	Description
A	Cell cross-section area, cm^2
δ	Electrode thickness, cm
c_{ref}	Reference H^+ concentration, mol/cm^3
$\bar{c}$	Average H^+ concentration, mol/cm^3
R	Universal gas constant, $J \cdot mol^{-1} \cdot K^{-1}$
F	Faraday's constant, C/mol
T	Temperature, K
R_f	Contact resistance, Ω
$\widetilde{U}_{PbO_2}$	Setpoint OCV slope, $V \cdot mol^{-1} cm^3$
C_{dl}	Double layer specific capacitance, C/cm^3
ε	Electrolyte volume fraction
a_c	Charge specific interfacial area, cm^2/cm^3
i_0	Exchange current density, A/cm^2
α_a	Anodic transfer coefficient
α_c	Cathodic transfer coefficient
γ	Butler-Volmer exponent
a_{dl}	double layer specific surface area, cm^2/cm^3

for full discharge, $Q = FA\varepsilon\delta\Delta c$ is the Ah capacity, and $\tau_{dl} = A\delta a_{dl} R_c C_{dl}$ is the equivalent double layer time constant. The parameters are provided in Tab. 4.1.

Many of the parameters in Tab. 4.1 are known (A, F, R, T, $\widetilde{U}_{PbO_2}$, δ) and do not change with battery age. The ohmic resistance, however, does increase with age due to the increased impedance and reduced power of aged batteries. If R_f is estimated from voltage and current data then the estimate $\hat{R}_f$ can be directly used as a State-Of-Power estimate and correlated to SOH.

For a direct SOH estimate, the capacity estimate

$$\hat{Q} = \frac{\hat{a}_1}{\hat{b}_0 \widetilde{U}_{PbO_2} \Delta c},$$

where the coefficients $\hat{a}_1$ and $\hat{b}_0$ are estimated using the LSM. In addition, the equivalent double layer time constant

$$\hat{\tau}_{dl} = \frac{1}{\hat{a}_1}$$

and equivalent charge transfer resistance

$$\hat{R}_c = \frac{\left(\hat{b}_1 - \frac{\hat{b}_0}{\hat{a}_1}\right)}{\hat{a}_1} - \hat{b}_2$$

can be estimated but their relationships to SOH and SOP are unknown.

4.2 Least Squares Method

For the second-order battery model in Eq. (4.1), estimates of coefficients a_i and b_i can be related to parameter estimates that can then be correlated to SOH and SOP. LSM is a system identification technique for linear and time-invariant models that estimates the coefficients in Eq. (4.1) that optimally fit the time-domain current and voltage data [3].

Figure 5.2 shows a schematic diagram of the LSM. Two identical low-pass filters filters input the current $I(t)$ and voltage $V(t)$ signals and output the filtered state vectors as follows

$$\dot{\mathbf{w}}_1 = \mathbf{F}\mathbf{w}_1 + \mathbf{b}_f I(t), \tag{4.2}$$

$$\dot{\mathbf{w}}_2 = \mathbf{F}\mathbf{w}_2 + \mathbf{b}_f V(t), \tag{4.3}$$

where

$$\mathbf{F} = \begin{bmatrix} 0 & 1 & 0 \\ 0 & 0 & 1 \\ -\lambda^3 & -3\lambda^2 & -3\lambda \end{bmatrix}, \ \mathbf{b}_f = \begin{bmatrix} 0 \\ 0 \\ 1 \end{bmatrix}.$$

The eigenvalues of $\mathbf{F}$ equal $\lambda > 0$, the bandwidth of the state filter. The states $\mathbf{w}_1$ and w_2 are filtered derivates of current and voltage, respectively,

$$\frac{\mathbf{W}_1(s)}{I(s)} = \frac{1}{s^3 + 3\lambda s^2 + 3\lambda^2 s + \lambda^3} \begin{bmatrix} 1 \\ s \\ s^2 \end{bmatrix}, \tag{4.4}$$

$$\frac{W_2(s)}{V(s)} = \frac{s}{s^3 + 3\lambda s^2 + 3\lambda^2 s + \lambda^3}, \tag{4.5}$$

Let $\mathbf{W}^T(s) = \left[\mathbf{W}_1^T(s),\ W_2(s)\right]$ and $\mathbf{\Theta}^T = [b_0,\ b_1,\ b_2,\ -a_1]$ and

$$\mathbf{\Theta}^T\mathbf{W}(s) = \frac{b_0 + b_1 s + b_2 s^2}{s^3 + 3\lambda s^2 + 3\lambda^2 s + \lambda^3} I(s) + \frac{a_1 s}{s^3 + 3\lambda s^2 + 3\lambda^2 s + \lambda^3} V(s). \quad (4.6)$$

By plugging Eq. (4.1) into Eq. (5.3), we obtain

$$\mathbf{\Theta}^T\mathbf{W}(s) = \frac{s^2}{s^3 + 3\lambda s^2 + 3\lambda^2 s + \lambda^3} V(s) = Z(s),$$

or, in the time domain,

$$z(t) = \mathbf{\Theta}^T\mathbf{w}(t).$$

The filter outputs are sampled periodically to produce

$$\mathbf{J} = [\mathbf{w}(0),\ \mathbf{w}(\Delta t),\ ...,\ \mathbf{w}((N_{eval} - 1)\Delta t)] \in \mathbb{R}^{4\times N_{eval}}$$

and $\mathbf{z} = [z(0),\ z(\Delta t),\ ...,\ z((N_{eval} - 1)\Delta t)] \in \mathbb{R}^{N_{eval}}$.

We can minimize the parameter estimation error function $e = \left(\mathbf{z} - \hat{\mathbf{\Theta}}^T\mathbf{J}\right)^2$ by choosing the least squares parameter estimate

$$\hat{\mathbf{\Theta}} = \left[\mathbf{J}\mathbf{J}^T\right]^{-1}\mathbf{J}\mathbf{z}. \quad (4.7)$$

4.3 Experimental Results

In the experiment, we test three AGM, VRLA batteries at different stages of life (new, aged, and dead) with different capacities (100Ah, 69Ah, and 49Ah, respectively) corresponding to different SOH (100%, 69%, and 49%, respectively). Each battery has six cells in series and the batteries have been modified so the voltages of all cells can be independently measured. The batteries are charged and discharged using a Techron LVC 5050 linear amplifier controlled with Simulink through a dSPACE interface board [77].

Before testing, the batteries are charged to 39% SOC and rested for over 10 hours. The testing data used for LSM SOH estimation consists of the sampled voltage response to a four minute 6.5 A (0.065C) charge pulse followed by four minutes of rest (See Fig. 4.2(d)). The sampled voltage and current data are

digitally filtered and passed through the LSM algorithm to produce the estimates $\hat{b}_0$, $\hat{b}_1$, $\hat{b}_2$, and $\hat{a}_1$ and the corresponding $\hat{R}_f$, $\hat{Q}$, $\hat{\tau}_{dl}$, and $\hat{R}_c$.

Figure 4.2 shows the experimental voltage response to the current input in (d) for the new (a), aged (b) and dead (c) batteries. The voltage starts at 2.01 V corresponding to 39% SOC and jumps immediately due to the current pulse initiation and the cell's ohmic resistance. During the charge pulse, the voltage increases due to charging of the double layer and conversion of active material. At the end of the pulse the voltage jumps down quickly and then transients to an almost steady state voltage of 2.02-2.03 V corresponding to a slightly higher SOC (about 41 - 44%). True steady state requires a much longer rest period (>1 - 2hr), however.

The new battery (a) shows the best match between the experimental and identified model simulation. The LSM accurately captures the ohmic jumps, transient shape, and SOC change.

Model identification error can be calculated using the Root Mean Square (RMS) of the voltage prediction error,

$$RMS_V = \sqrt{\frac{1}{N_{eval}} \sum_{i=0}^{N_{eval}-1} \left(\hat{V}\left((i-1)\,\Delta t\right) - V\left((i-1)\,\Delta t\right) \right)^2},$$

and $\hat{V}(t)$ is the voltage predicted by simulation of Eq. (4.1) with LSM parameter estimates and zero initial conditions. The measurement noise is a small contribution ($RMS \approx 1$ mV) to the overall RMS_V.

The RMS_V for the new cell of 1.554 mV is a small percentage (2.1%) of the overall voltage swing (75 mV), demonstrating the accuracy of the LSM parameter identification and the second order model itself. The $RMS_V = 4.462$ mV of the aged cell and visual inspection of the responses indicate a poorer fit of the identified model. The LSM method has done its best to fit the second order model to the aged voltage data but has come up short. The second order model no longer represents the cell dynamics due to aging.

The dead battery has the largest $RMS_V = 9.648$ mV and the identified voltage response does a poor job of tracking the experimental voltage. One reason for increased identification errors in aged cells is the accumulation of lead sulfate

in the porous electrodes. In a rested cell, lead sulfate can block pores and their opening up during the initial charge pulse creates a transient that the second order model cannot match accurately. This is the well known coup-de-fouet mechanism for lead acid batteries that has been correlated to SOH [49, 46]. This coup-de-fouet mechanism also manifests itself with initial pulse transients for a rested cell that differ from subsequent transients. Figure 4.3 compares the experimental voltage responses of the new and dead cells to multiple charge and discharge pulses. The voltage responses to the two charge pulses are similar for the new cell but very different for the dead cell. During the second charge pulse, the dead cell is closer to a second order system and RMS_V decreases. Before the experiment, the cells have been at rest for over 10 hours, during which lead sulfate can partially block the electrode pores through dissolution and recrystalization. Heterogeneous distributions of active materials and crystals can block pores in aged cells. During the first charge pulse, acid is produced in the blocked pores but it cannot flow out. Eventually, the pore-blocking active materials are consumed, the pores open, electrolyte diffusion is enabled, and the voltage responds similar to new cells. Another explanation is that lead sulfate crystals with stiff and smooth surfaces require higher voltage to start the charge reaction, causing different voltage responses between the first and subsequent pulses in the aged and dead cells.

The identification results provide three possible methods of estimating SOH and SOP from experimental voltage and current data. First, the LSM generates $\hat{Q}$ and $\hat{R}_f$, the least squares optimal estimate of the cell capacity and ohmic resistance, which are proportional and inversely proportional to SOH and SOP, respectively. Second, the LSM generates $\hat{\tau}_{dl}$ and $\hat{R}_c$ that may be correlated to SOH and/or SOP. Finally, the estimation error for the first pulse after resting increases with age and may be correlated to SOH and SOP.

To investigate the performance of these estimation methods, we compare the parameter estimates and estimate errors for all six cells of the fresh, aged, and dead batteries. The percentage changes are calculated from the average of the six fresh cells of $\hat{R}_{f0}$, $\hat{\tau}_{dl0}$, $\hat{R}_{c0}$, $\hat{Q}_0$, and RMS_{V0}. Figure 4.4 plots the parameter estimates $\hat{R}_f$, $\hat{Q}$, $\hat{\tau}_{dl}$, and $\hat{R}_c$ versus RMS_V for the 18 cells tested. The RMS_V values are the same in all four plots, showing a clear trend with age. The fresh cell RMS_V are tightly clustered, ranging from -2.61% to 2.58% error. The aged cells

have markedly higher and wider-ranging RMS_V from 12.29% to 180.60%. The dead cells have the highest RMS_V (303.48% to 592.56%). Clearly, RMS_V is a very sensitive SOH indicator for Lead-Acid cells. In addition, the RMS_V results show that parameter estimates for the aged and dead cells may be unreliable due to the large estimation errors.

Figure 4.4 (a) shows that the cell ohmic resistance estimates $\hat{R}_f$ increase steadily with age. This expected result indicates that $\hat{R}_f$ can be used as a SOP estimate. Cell capacity estimates $\hat{Q}$ decrease by 34% on average from the fresh cells to the aged cells, matching the 31% decrease in the measured capacity from 100 Ah to 69 Ah. The average $\hat{Q}$ of the dead cells is only 6% less than the aged cells but the measured capacity decreases by 20%. This demonstrates that $\hat{Q}$ is more sensitive to estimation error than $\hat{R}_f$. Thus, $\hat{Q}$ is not a reliable SOH estimator at high RMS_V. The equivalent double layer capacitance estimate $\hat{\tau}_{dl}$ does not show a monotonic trend with age, decreasing from the fresh to the aged cells and then increasing from the aged to the dead cells. This may be due to different degradation (*e.g.* sulfation versus water loss) that dominate the degradation in the aged and dead cells or simply an artifact of the high estimation error. Equivalent charge transfer resistance estimates $\hat{R}_c$ varies little and non-monotonically with age, so it is not a useful SOH or SOP estimator.

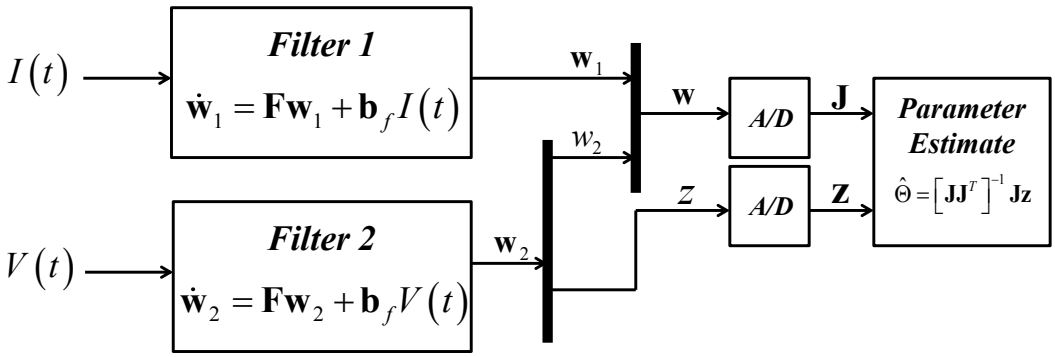

Figure 4.1. Schematic Diagram of the Least Squares Method

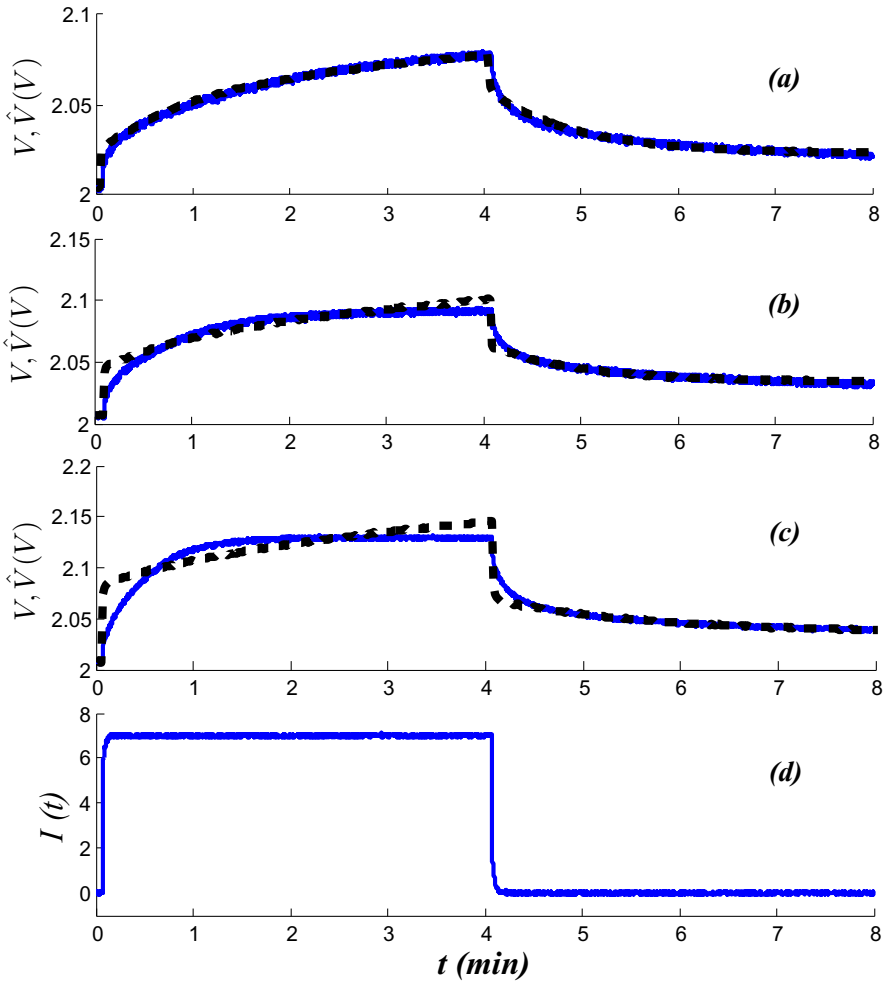

Figure 4.2. Experimental cell 5 voltage response (solid) and the identified model simulation (dashed) for the (a) new battery ($RMS_V = 1.554$ mV), (b) aged battery ($RMS_V = 4.462$ mV), and (c) dead battery (($RMS_V = 9.648$ mV)) to the input current (d).

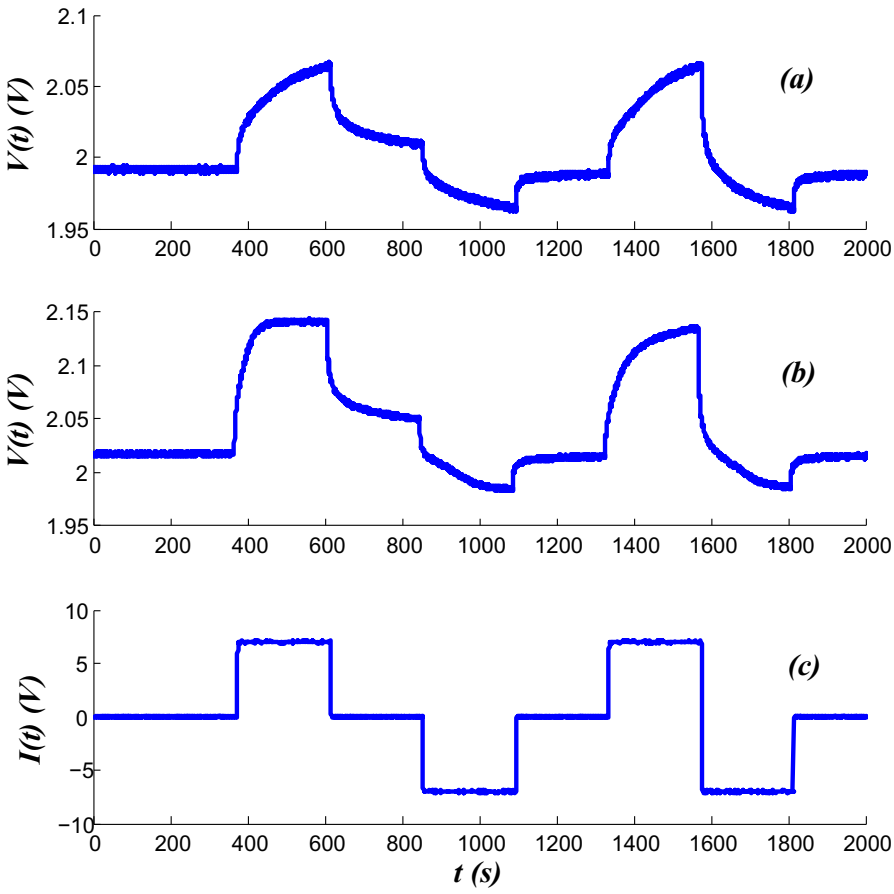

Figure 4.3. Experimental voltage response of the new cell (a) and the dead cell (b), to the input current (c) the current input.

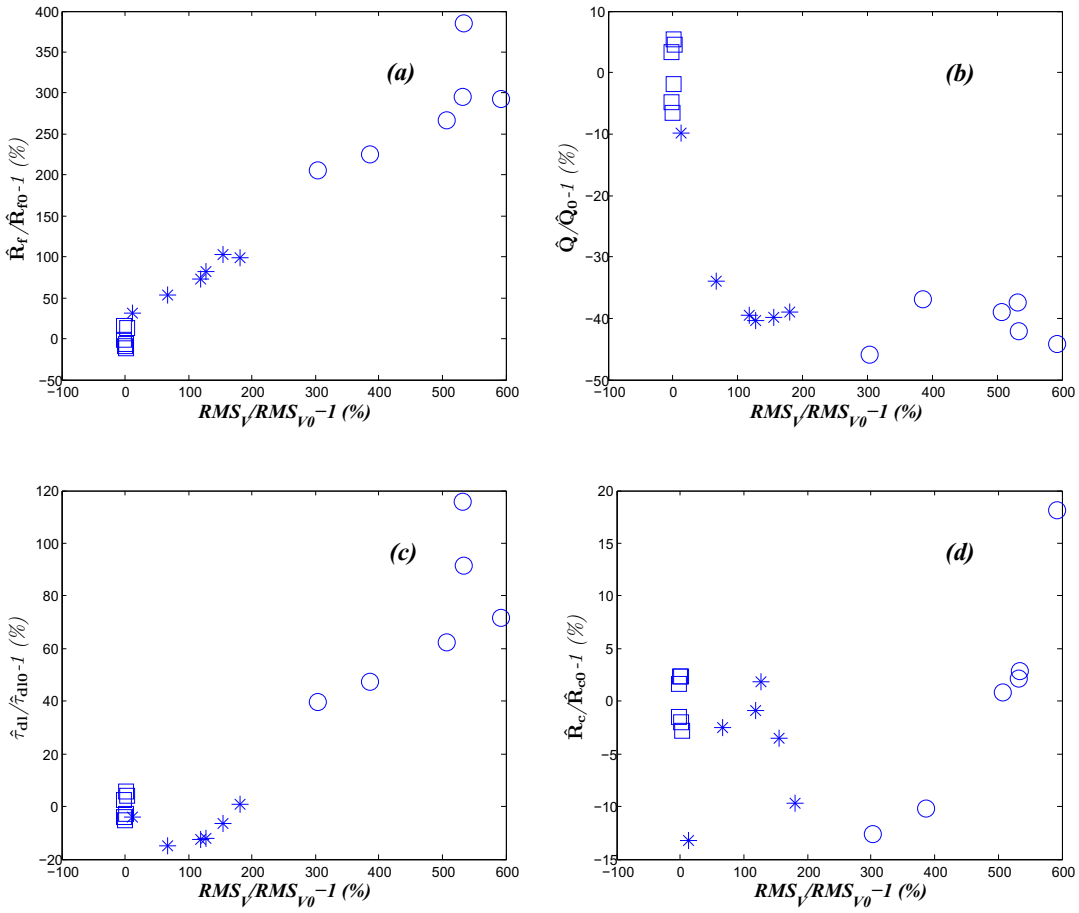

Figure 4.4. Parameter estimation errors versus voltage estimation error RMS_V versus parameter estimates for the new (□), aged (⋆), and dead (o) battery cells: (a) ohmic resistance estimate, $\hat{R}_f$, (b) capacity estimate, $\hat{Q}$, (c) equivalent double layer time constant estimate, $\hat{\tau}_{dl}$, and (d) charge transfer resistance estimate, $\hat{R}_c$.

Chapter 5

Parameter Estimation: Solid Phase Diffusivity Measurement

In this chapter, we extend the LSM to estimate battery parameters that vary with SOC and operating condition. Solid phase diffusivity (D_s) is an important parameter that dominates the dynamics of Li-Ion cells. To accurately measure D_s, the LSM is applied to a Galvanostatic Intermittent Titration Technique (GITT) test data to develop the Least Squares GITT (LS-GITT) method. The accuracies of LS-GITT and GITT are evaluated with their voltage estimate error RMS. LS-GITT is shown to be more accurate than GITT in a wide range of SOC.

5.1 Model Development for Solid Phase Diffusivity Measurement of a Li-Ion Cell

Figure 5.1 shows the half cell model with a NCM positive electrode and a metal Lithium negative electrode. The model assumes that: (i) the NCM material is modeled by a single solid phase spherical particle with radius R_s; (ii) $\mathbf{Li}^+$ transport in the electrolyte is neglected; (iii) the discharge rate is low; (iv) the SOC change is small for each pulse; and (v) isothermal conditions apply. Assumptions (i) and (ii) are also used in the widely accepted Single Particle Model (SPM) [78]. Assumptions (iii) - (v) are reasonable for the low C-rate GITT current input.

In [56], a reduced-order Li-Ion cell model is developed using the Padé Ap-

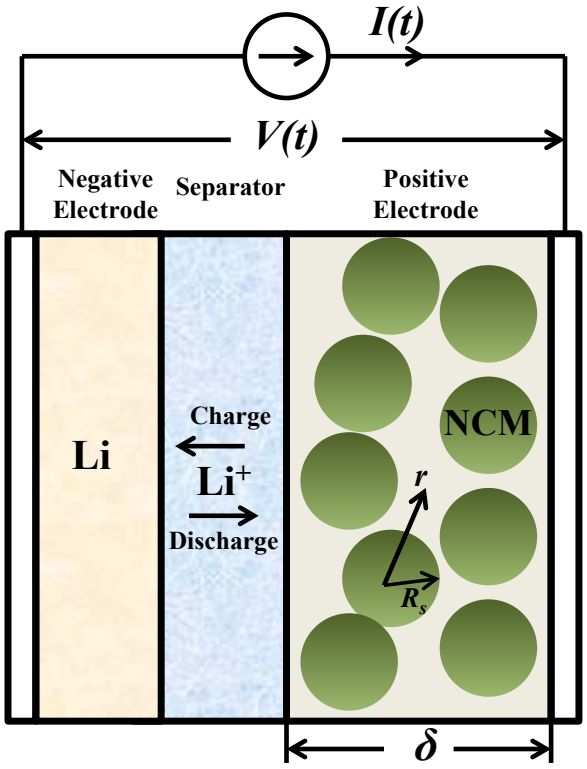

Figure 5.1. Schematic diagram of the half cell model

proximation [14, 15], with the impedance transfer function coefficients explicitly correlated to physical and electrochemical parameters of the cell. For half cells, the same approach produces the second-order impedance transfer function:

$$\frac{V(s)}{I(s)} = \frac{R_T s^2 + (35 R_T \alpha_2 + 10\alpha_1)\, s + 105\alpha_1\alpha_2}{s^2 + 35\alpha_2 s}, \tag{5.1}$$

where $\alpha_1 = \frac{C_+}{3AF\delta\varepsilon_s}$, $\alpha_2 = \frac{D_s}{R_s^2}$, and total resistance $R_T = R_f + \frac{R_{ct}}{a_s A\delta}$, with $R_{ct} = \frac{RT}{i_0 F(\alpha_a+\alpha_c)}$. The parameters are described in Tab. 5.1. If α_2 and R_s are known, then D_s can be calculated.

Table 5.1. Model Parameters model

Parameter	Description
A	Cell cross-section area, cm^2
δ	Positive electrode thickness, cm
R	Universal gas constant, $J \cdot mol^{-1} \cdot K^{-1}$
F	Faraday's constant, C/mol
T	Temperature, K
R_f	contact resistance, Ω
C_+	Setpoint OCV slope, $V \cdot mol^{-1} cm^3$
ε_s	Solid phase volume fraction
a_s	Specific solid phase area, cm^2/cm^3
i_0	Exchange current density, A/cm^2
α_a	Anodic transfer coefficient
α_c	Cathodic transfer coefficient

5.2 Least Squares Galvanostatic Intermittent Titration Technique

For the second-order battery model in Eq. (5.1), the impedance transfer function of the cell is in the following form:

$$\frac{V(s)}{I(s)} = \frac{b_2 s^2 + b_1 s + b_0}{s^2 + a_1 s}, \tag{5.2}$$

where the coefficients a_i and b_i are related to the parameters of the cell, including D_s. If a_1 is known, for example, $D_s = a_1 R_s^2/35$.

The Least Squares Method (LSM) is a system identification technique for linear and time-invariant models that estimates the coefficients in Eq. (5.2) that optimally fit the time-domain current and voltage data [3]. By applying the LSM to the GITT current and voltage data, we develop a new D_s estimation method, the Least Squares Galvanostatic Intermittent Titration Technique (LS-GITT).

Figure 5.2 shows a diagram of the LS-GITT algorithm. Two digital low-pass filters process the N_{eval} current $\mathbf{I}$ and voltage $\mathbf{V}$ data points from a single current pulse to produce filtered current $\hat{\mathbf{I}}$, $\hat{\dot{\mathbf{I}}}$, and $\hat{\ddot{\mathbf{I}}}$, and voltage $\hat{\dot{\mathbf{V}}}$ and $\hat{\ddot{\mathbf{V}}}$ derivatives. The filter bandwidth is $\lambda(rad/s)$.

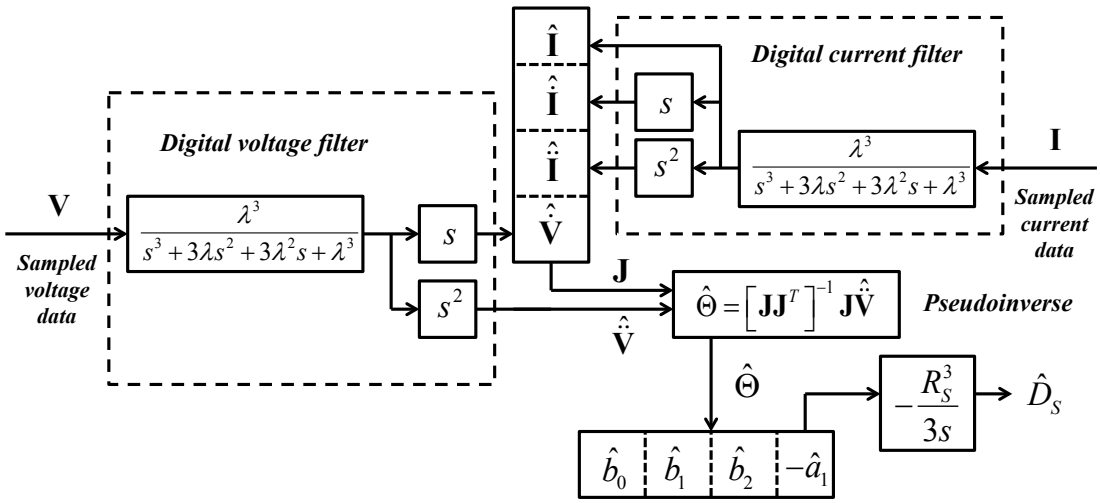

Figure 5.2. Block Diagram of the LS-GITT algorithm

Let $\mathbf{W}^T(s) = \left[\hat{I}(s), \hat{\dot{I}}(s), \hat{\ddot{I}}(s), \hat{\dot{V}}(s)\right]$ and $\mathbf{\Theta}^T = [b_0,\ b_1,\ b_2,\ -a_1]$ so

$$\mathbf{\Theta}^T\mathbf{W}(s) = \frac{b_0 + b_1 s + b_2 s^2}{s^3 + 3\lambda s^2 + 3\lambda^2 s + \lambda^3} I(s) + \frac{a_1 s}{s^3 + 3\lambda s^2 + 3\lambda^2 s + \lambda^3} V(s). \qquad (5.3)$$

Substitution of Eq. (5.2) into Eq. (5.3) produces

$$\mathbf{\Theta}^T\mathbf{W}(s) = \frac{s^2}{s^3 + 3\lambda s^2 + 3\lambda^2 s + \lambda^3} V(s) = \hat{\ddot{V}}(s),$$

or, in the time domain,

$$\hat{\ddot{V}}(t) = \mathbf{\Theta}^T\mathbf{w}(t).$$

The digital filter outputs are stacked into

$$\mathbf{J} = [\mathbf{w}(0),\ \mathbf{w}(\Delta t),\ ...,\ \mathbf{w}((N_{eval} - 1)\Delta t)] \in \mathbb{R}^{4\times N_{eval}}$$

and $\hat{\ddot{\mathbf{V}}} = \left[\hat{\ddot{V}}(0),\ \hat{\ddot{V}}(\Delta t),\ ...,\ \hat{\ddot{V}}((N_{eval} - 1)\Delta t)\right] \in \mathbb{R}^{N_{eval}}$.

For the GITT diffusivity measurements, V_0, ..., V_3 are determined from the voltage data for each pulse and substituted into Eq. (1.5) to calculate D_s. For the LS-GITT diffusivity measurements, the current and voltage data are passed into 40 pulse inputs and outputs. Each set of pulse data is then processed through the LS-GITT algorithm to produce D_s.

We can minimize the parameter estimation error function $e = \left(\hat{\dot{\mathbf{V}}} - \hat{\boldsymbol{\Theta}}^T \mathbf{J}\right)^2$ by choosing the pseudoinverse

$$\hat{\boldsymbol{\Theta}} = \left[\mathbf{J}\mathbf{J}^T\right]^{-1} \mathbf{J}\hat{\dot{\mathbf{V}}}. \tag{5.4}$$

5.3 Diffusivity Measurement Results using GITT and LS-GITT

Figure 5.3 compares the diffusivity measurements (a) and accuracies (b) of LS-GITT and GITT using the current and voltage data in Fig. 1.2. Figure 5.3(a) shows that the D_s measurements range from $10^{-10} - 10^{-11}$ cm^2/s at $SOC > 10\%$, matching published results in the literature [57]. LS-GITT loses stability at extremely low SOC ($< 5\%$) and the D_s estimate jumps dramatically and becomes negative. GITT is more stable and always produces positive D_s measurements.

Figure 5.3(b) evaluates the D_s measurement accuracy of GITT and LS-GITT using the RMS_{GITT} in Eq. (1.6) and

$$RMS_{LS} = \sqrt{\frac{1}{N_{eval}} \sum_{i=0}^{N_{eval}-1} \left(\hat{V}\left(\left(i-1\right)\Delta t\right) - V\left(\left(i-1\right)\Delta t\right)\right)^2},$$

where $\hat{V}(t)$ is the voltage predicted by simulation of Eq.(5.2) with LS-GITT parameters estimates. At $SOC > 10\%$ (first 36 discharge pulses), $RMS_{LS} < RMS_{GITT}$ so the LS-GITT method is more accurate than GITT. Both methods have very high $RMS_V > 10$ mV because they fail to match experimental voltage data at low SOC. Even though GITT produces D_s measurements at $SOC < 5\%$, they are inaccurate and of questionable utility. GITT D_s measurements are not as accurate as LS-GITT for most SOC. In fact, from 60% - 100% SOC LS-GITT is almost an order of magnitude more accurate than GITT. If we set a RMS accuracy cutoff of 1 mV (roughly the RMS noise of the voltage sensor), then the LS-GITT has a working range of (15% - 100%), more than double than the GITT working range of (20% - 60%).

Figure 5.4 shows representative pulse responses at 100% (a), 50% (b), and 2.5% (c) SOC. The voltage prediction of the LS-GITT model matches the experimental

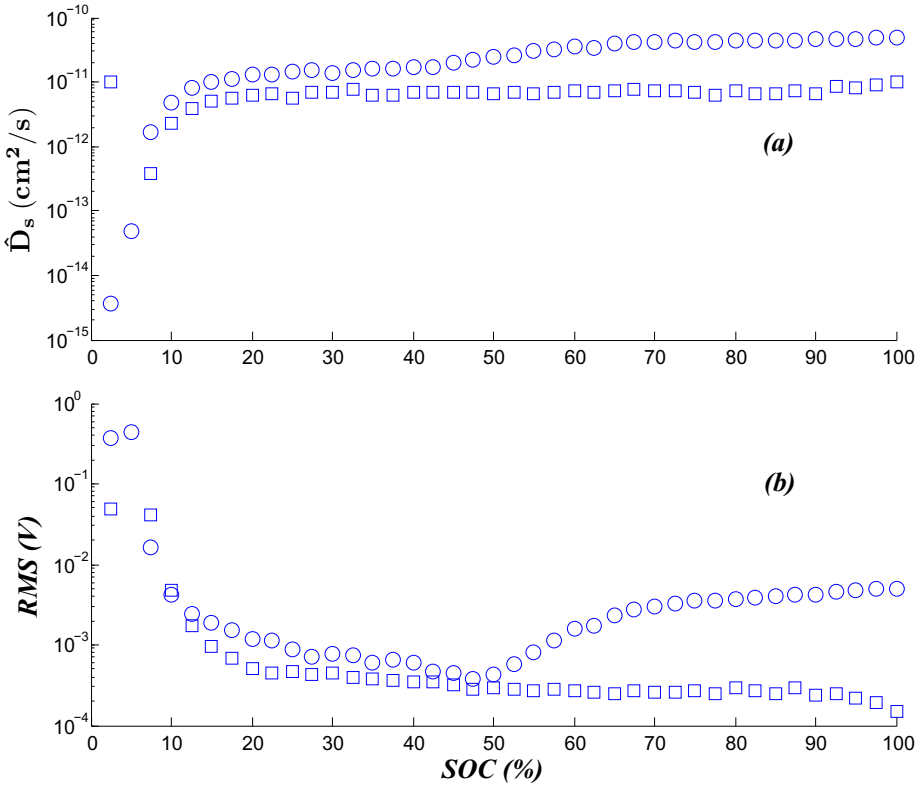

Figure 5.3. Measured diffusivities $\hat{D}_s$ (a) and RMS estimation errors (b) versus SOC for GITT (o) and LS-GITT (□).

voltage data well ($RMS_{LS} = 0.1489$ mV) but the GITT voltage estimate deviates considerably from the experimental data ($RMS_{GITT} = 5.085$ mV). The GITT simulation passes through the points V_1 and V_2 exactly because they are inputs to the GITT formula. The transient response between V_1 and V_2, however, is not accurately captured by the model. The LS-GITT response, on the other hand, accurately matches the ohmic drop and rise at the start and end of the discharge pulse, respectively, the transients during and after the pulse, and the steady state response. Clearly, the LS-GITT model more accurately fits the experimental data. So the corresponding diffusivity is an accurate measurement. The GITT diffusivity measurement is dubious at best. At 50% SOC, both methods produce accurate measurements of diffusivity as measured by the RMS error. Visual inspection of Fig. 5.4(b) also shows excellent agreement between the models and the experiment. It is interesting to note, however, that the models predict different diffusivities (LS-

GITT $D_s = 6.92 \times 10^{-12}$ cm^2/s and GITT $D_s = 2.23 \times 10^{-11}$ cm^2/s). The LS-GITT has a smaller $RMS_{LS} = 0.2934$ mV as compared to $RMS_{GITT} = 0.4349$ mV so it should be closer to the actual value. Or we could conclude that the actual value lies somewhere between 6.92×10^{-12} and 2.23×10^{-11} cm^2/s.

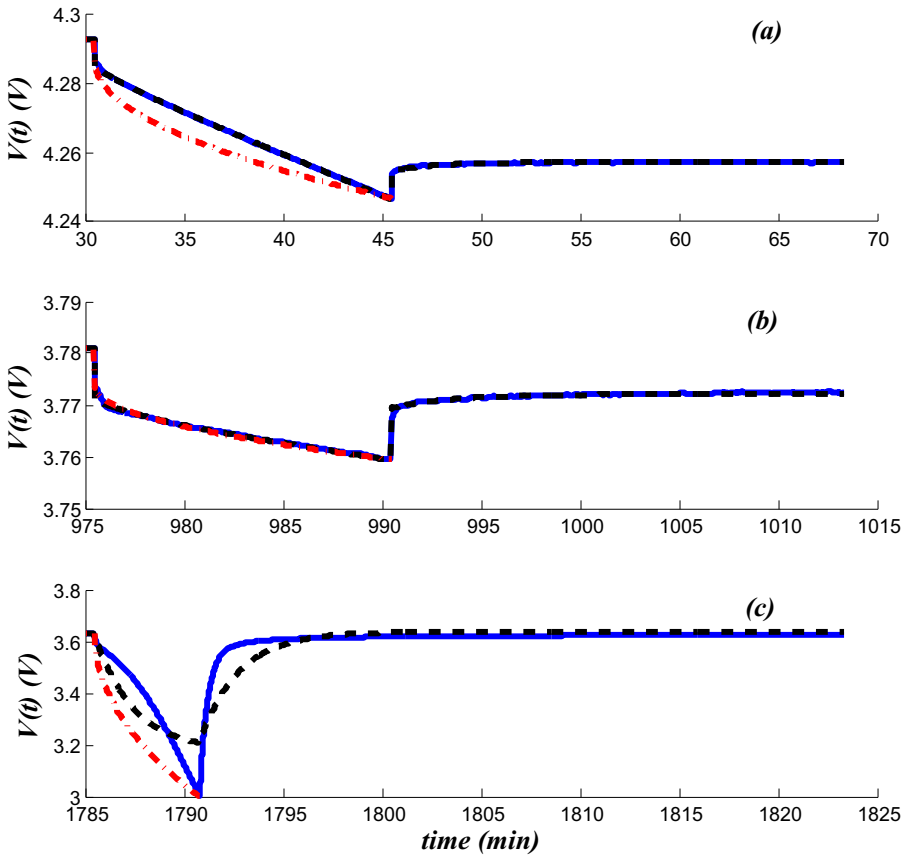

Figure 5.4. Voltage response versus time (experimental (solid), GITT model simulation (dash-dotted), and LS-GITT model simulation (dashed)): (a) 100% SOC, (b) 50% SOC, (c) 2.5% SOC.

Figure 5.4(c) shows that neither model matches the experimental response at 2.5% SOC. It is impossible for either model to have the concave transient exhibitted in the experiment. Despite the low C-rate and small pulses, $\frac{dV}{d\gamma} \neq \frac{\Delta V}{\Delta \gamma}$, violating a GITT assumption and $\frac{dV}{d\gamma} \neq$constant, violating an LS-GITT assumption. The large errors associated with these measurements mean that neither can be considered accurate. Although the data time length is the same as the other 39 pulses, the discharge pulse ends prematurely at the low voltage cutoff (3V).

Chapter 6

Conclusions and Future Work

6.1 Conclusions

In this research, we present a reduced-order physics-based model of a Pb-Acid battery based on a linearized, coupled partial differential equations using an efficient Ritz discretization method. Experiments show that the Pb-Acid battery has different dynamics for charge and discharge. A switching law σ is designed to approximate the model switching between charge and discharge, making the Ritz model a switched linear system. The Ritz model is able to output crucial internal and external variables, such as acid concentration, electrolyte potential, solid-phase potential, and voltage. The fast convergence of the Ritz method enables a low-order model to closely match the experimental voltage response. The dynamic averaged model is a low-order Ritz model that is realized by an equivalent circuit. The circuit component values such as resistance and capacitance can be explained and calculated from the electrochemical parameters of the underlying Pb-Acid battery model, bridging the gap between equivalent circuit and first principles models.

We also design SOC estimators based on 5 VRLA battery models and compares them with the Voltage Lookup method. The two switched linear models predict the SOC and voltage better than the three linear models that do not include switching and all of the estimators outperform the Voltage Lookup method. A LMI-based design method is used to obtain an optimal switched SOC estimator with guaranteed exponential stability. The switched SOC estimator based on a

low-pass-filtered switching law converges smoothly and is the most accurate, especially when the input current changes quickly. All of the estimators perform worse if operated far from the linearization point (SOC), so gain scheduling would be recommended for large SOC operating ranges.

The Least Squares Method based on a second order model of Lead-Acid batteries can provide reliable estimates of SOH and SOP. The ohmic resistance estimate increases monotonically with age, providing an estimate of SOP. The capacity estimate decreases monotonically with age, matching the actual capacity loss for aged cells. Finally, the voltage estimate error can be used as a SOH/SOP estimator and quantify the reliability of the parameter estimates. The first pulse after a long rest period shows the highest estimation error.

Based on experimental results from a NCM half cell, LS-GITT is more accurate than GITT, sometimes by several orders of magnitude. LS-GITT gives results accurate to 1 mV RMS from 15% - 100% SOC where GITT provides that level of accuracy over less than half that range. Neither technique provides accurate D_s measurements below 10% SOC.

6.2 Future Work

6.2.1 Extended Applications of LS-GITT

Two extended applications of LS-GITT are promising in the measurement of other cell parameters or parameters in other Li-Ion chemistries.

Firstly, the second order Lithium Ion half cell model Eq. (5.1) has three independent coefficients $\alpha_1 = \frac{C_+}{3AF\delta\varepsilon_s}$, $\alpha_2 = \frac{D_s}{R_s^2}$, and total resistance $R_T = R_f + \frac{R_{ct}}{a_s A\delta}$, with $R_{ct} = \frac{RT}{i_0 F(\alpha_a+\alpha_c)}$. α_2 has been used for solid phase diffusivity measurement. α_1 is correlated the setpoint OCV slope and potentially useful for SOH estimation. R_T is the sum of ohmic resistance and charge transfer resistance. Charge transfer resistance R_{ct} can be used for the measurement of exchange current density i_0, an important electrochemical parameter. The LS-GITT already provides estimates of R_T, then R_{ct} can be separated from R_T by measuring ohmic resistance R_f using high frequency resistance test or Electrochemical Impedance Spectroscopy (EIS).

Secondly, solid phase diffusivity in phase change electrode materials, such as

lithium iron phosphate and lithium titanium oxide, are almost impossible to measure using GITT due to flat OCV versus SOC curves. Unlike GITT, the feasibility of LS-GITT is not impacted by $\Delta V_s \approx 0$ in Eq. (1.5). Model Eq. (5.1) cannot be directly used for phase change materials because the model equations are different due to difference in electrochemical mechanism. However, we can still generate transfer function models by discretizing previously published electrochemical models [79] using Padé Approximation [14, 15]. After that, LS-GITT algorithm can be employed to measure D_s and other parameters in a phase change Li-Ion cell.

6.2.2 SOC-Based Battery Balancing

SOC-based battery balancing is another promising direction for future research. In battery packs, batteries are often connected in series to satisfy voltage and power requirements. Unfortunately, the imbalance of SOC among the batteries occurs due to the discrepancies in capacity, impedance, and working conditions such as ambient temperature [80]. Battery imbalance is one of the greatest enemies of the battery systems, because it causes overcharge and overdischarge in the battery, and a single 'weak' battery often limit the performance and cycle life of the whole battery pack [81]. Moreover, imbalance deteriorates if no measure is taken to equalize the batteries, motivating battery balancing.

Battery balancing techniques have been developing for decades and helping to extend the cycle life of battery packs. They are designed to equalize the voltage instead of the SOC of the batteries, so imbalances actually occur since the parameters (especially ohmic resistances) vary in different batteries. Based on the SOC estimator designed in Chapter 3, we can study the battery balancing problem from a new perspective: SOC balancing.

Several tasks need to be done for this research. Firstly, parameter estimation methods are needed to customize models for different batteries. Often, exact models for different batteries are not available, and we will start from measuring the contact resistances, to which the error of voltage-based methods is mostly attributed. Secondly, active balancing circuits based on SOC need to be designed, which can be extended from the battery testbed [77] by adding more channels for balancing current. Thirdly, experiments are needed to compare voltage-based and

SOC-based balancing methods.

6.2.3 SOH estimation of aged batteries using data-driven methods

In Chapter 4, SOH-related parameter estimate accuracy decreases with the age of the battery, especially the estimates of charge transfer resistance R_c and double layer time constant τ. As the battery ages, the experimental voltage and current data of aged cells deviate from a known model due to unmodeled dynamics, so model-based methods such as LSM no longer provides accurate parameter estimation.

Data-driven methods [82], on the other hand, can robustly and adaptively estimate parameters in aged cells if enough data is available. Data-driven methods, for instances, Machine Learning [83, 84], Adaptive Control [85, 86], and Symbolic Dynamic Filtering (SDF) [87, 88, 89, 90] have been proposed and developing rapidly with the advances of computer technology. SDF is a powerful parameter estimation and pattern recognition method for early detection of anomalies (i.e., deviations from the normal behavior), parametric and nonparametric changes in dynamic systems. SDF processes time series data and constructs state machines with state probability vector $\mathbf{p}$ through data space partitioning. $\mathbf{p}$ denotes the pattern of the dynamic system, and the relationship can be determined between $\mathbf{p}$ and SOH-related parameters through the training data. The change in $\mathbf{p}$ can be used as a SOH indicator, and the change in SOH-related parameters can be estimated more accurately than model-based methods. Interested readers are refered to [87].

In addition, we find increasingly divergent voltage responses amongst cells in the aged battery, and the discrepancies in cell responses can also be used for SOH estimation of batteries, providing another data-driven SOH estimation methodology worth considering for future research.

Appendix A

Table A.1. Ritz model matrix elements

Matrix	Integral form
$\mathbf{M}_e\,(n,m)$	$\int_0^{L_1} a_{dl}C_{dl}\Psi_n(x)\Psi_m(x)dx + \int_{L_2}^{L} a_{dl}C_{dl}\Psi_n(x)\Psi_m(x)dx$
$\mathbf{M}_{es}\,(n,1)$	$-\int_0^{L_1} a_{dl}C_{dl}\Psi_n(x)dx$
$\mathbf{M}_{es}\,(n,2)$	$-\int_{L_2}^{L} a_{dl}C_{dl}\Psi_n(x)dx$
$\mathbf{K}_e\,(n,m)$	$-\kappa^{\text{eff}}\int_0^L \Psi'_n(x)\Psi'_m(x)dx - \int_0^{L_1} R_a\Psi_n(x)\Psi_m(x)dx - \int_{L_2}^{L} R_a\Psi_n(x)\Psi_m(x)dx$
$\mathbf{K}_{ec}\,(n,m+1)$	$-\int_0^L \kappa_d^{\text{eff}}\Psi'_n(x)\Psi'_m(x)dx - \int_0^{L_1} R_a\widetilde{U}_{PbO_2}\Psi_n(x)\Psi_m(x)dx$
$\mathbf{K}_{es}\,(n,1)$	$\int_0^{L_1} R_a\Psi_n(x)dx$
$\mathbf{K}_{es}\,(n,2)$	$\int_{L_2}^{L} R_a\Psi_n(x)dx$
$\mathbf{B}_e(n,1)$	0
$\mathbf{B}_e\,(n,2)$	$-\int_0^{L_1} R_a\Psi_n(x)dx$
$\mathbf{M}_s$	$\begin{bmatrix} -a_{dl}C_{dl}L_1 & 0 \\ 0 & -a_{dl}C_{dl}\,(L-L_2) \end{bmatrix}$
$\mathbf{M}_{se}\,(1,n)$	$\int_0^{L_1} a_{dl}C_{dl}\Psi_n(x)dx$
$\mathbf{M}_{se}\,(2,n)$	$\int_{L_2}^{L} a_{dl}C_{dl}\Psi_n(x)dx$
$\mathbf{K}_{sc}\,(1,n+1)$	$-\int_0^{L_1} R_a\widetilde{U}_{PbO_2}\Psi_n(x)dx$
$\mathbf{K}_{sc}\,(2,n)$	0
$\mathbf{K}_{se}\,(1,n)$	$-\int_0^{L_1} R_a\Psi_n(x)dx$
$\mathbf{K}_{se}\,(2,n)$	$-\int_{L_2}^{L} R_a\Psi_n(x)dx$
$\mathbf{K}_s$	$\begin{bmatrix} R_aL_1 & 0 \\ 0 & R_a\,(L-L_2) \end{bmatrix}$
$\mathbf{B}_s$	$\begin{bmatrix} -\frac{1}{A} & -R_aL_1 \\ \frac{1}{A} & 0 \end{bmatrix}$
$\mathbf{M}_c\,(n+1,m+1)$	$\int_0^L \varepsilon\Psi_n(x)\Psi_m(x)dx$
$\mathbf{K}_c\,(n+1,m+1)$	$-\int_0^L D^{\text{eff}}\Psi'_n(x)\Psi'_m(x)dx - \widetilde{U}_{PbO_2}\int_0^{L_1}\frac{a_2R_a}{2F}\Psi_n(x)\Psi_m(x)dx$
$\mathbf{K}_{ce}\,(n+1,m)$	$-\int_0^{L_1}\frac{a_2R_a}{2F}\Psi_n(x)\Psi_m(x)dx - \int_{L_2}^{L}\frac{a_2R_a}{2F}\Psi_n(x)\Psi_m(x)dx$
$\mathbf{K}_{cs}\,(n+1,1)$	$\int_0^{L_1}\frac{a_2R_a}{2F}\Psi_n(x)dx$
$\mathbf{K}_{cs}\,(n+1,2)$	$\int_{L_2}^{L}\frac{a_2R_a}{2F}\Psi_n(x)dx$
$\mathbf{B}_c\,(n,1)$	0
$\mathbf{B}_c\,(n+1,2)$	$-\int_0^{L_1}\frac{a_2R_a}{2F}\Psi_n(x)dx$
$\int \Psi'_n\,(x)\,\Psi'_m\,(x)\,dx$	$\begin{cases} x & n=m=0 \\ \frac{L}{4n\pi}\sin\frac{2n\pi x}{L}+\frac{x}{2} & n=m\neq 0 \\ \frac{L}{2(n+m)\pi}\sin\frac{(n+m)\pi x}{L}+\frac{L}{2(n-m)\pi}\sin\frac{(n-m)\pi s}{L} & n\neq m \end{cases}$
$\int \Psi'_n\,(x)\,\Psi'_m\,(x)\,dx$	$\begin{cases} 0 & n \text{ or } m=0 \\ \frac{1}{2}\left(\frac{n\pi}{L}\right)^2\left(x-\frac{L}{2n\pi}\sin\frac{2n\pi x}{L}\right) & n=m\neq 0 \\ \frac{nm}{2}\left(\frac{\pi}{L}\right)^2\left[\frac{L}{(n-m)\pi}\sin\frac{(n-m)\pi x}{L}-\frac{L}{(n+m)\pi}\sin\frac{(n+m)\pi x}{L}\right] & n\neq m \end{cases}$

Appendix B

B.1 Direct design of Switched Luenberger Observer for the third-order Dynamic Averaged Model

The switched linear third order model given by Eq. (2.20) has two subsystems for charge and discharge separately. To design a Switched Luenberger Observer, we can start by designing Luenberger Observer for each subsystem. Each system has three poles: 0, $-\lambda_2$, and $-\lambda_4$, which is stable but not assymptotically stable. So, we can place the pole at 0 to $-\lambda_d$ and hence make the closed-loop subsystem assymptotically stable by using the following feedback matrix:

$$\mathbf{L} = \lambda_d \begin{bmatrix} \frac{1}{\widetilde{U}_{PbO_2}} \\ 1 \\ 0 \end{bmatrix}.$$

Then, the error dynamics of the subsystem is

$$\dot{\mathbf{e}} = \mathbf{A_{CL}}\mathbf{e}, \tag{B.1}$$

where

$$\mathbf{A_{CL}} = (\mathbf{A} - \mathbf{LC}) = \begin{bmatrix} 0 & -\frac{\lambda_d}{\widetilde{U}_{PbO_2}} & \frac{\lambda_d}{\widetilde{U}_{PbO_2}} \\ \widetilde{U}_{PbO_2}\lambda_2 & -(\lambda_2 + \lambda_d) & \lambda_d \\ 0 & 0 & -\lambda_4 \end{bmatrix}.$$

The characteristic polynomial of $\mathbf{A_{CL}}$ is $(s+\lambda_d)(s+\lambda_2)(s+\lambda_4)$, with all poles in the LHP of the s-plane. Therefore, feedback matrix $\mathbf{L}$ makes subsystem error dynamics Eq. (B.1) assymptotically stable. Furthermore, $\mathbf{L}$ is proportional to the desired pole $-\lambda_d$ and the same for both charge and discharge subsystems if same λ_d is needed for both subsystems, which is convenient for switched observer design.

The eigenvectors of $\mathbf{A_{CL}}$ are assembled into matrix $\mathbf{T}$ as below:

$$\mathbf{T} = \begin{bmatrix} 1 & \lambda_d & 1 \\ \widetilde{U}_{PbO_2} & \widetilde{U}_{PbO_2}\lambda_2 & \widetilde{U}_{PbO_2} \\ 0 & 0 & -\widetilde{U}_{PbO_2}\left(1+\frac{\lambda_4}{\lambda_d}\right) \end{bmatrix}$$

B.2 Error Dynamics Exponential Stability Proof

Error dynamics of subsystem i (1: charge, 2: discharge) is given by:

$$\dot{\mathbf{e}} = \mathbf{A_{CLi}}\mathbf{e},$$

where

$$\mathbf{A_{CLi}} = (\mathbf{A_i} - \mathbf{L_i}\mathbf{C_i})$$

Parameters $\lambda_2 = \frac{Ra_1}{a_{dl1}C_{dl1}}$ and $\lambda_4 = \frac{Ra_3}{a_{dl3}C_{dl3}}$ take on different values between charge and discharge, which are labeled λ_{2c} and λ_{4c} for charge and λ_{2d} and λ_{4d} for discharge. $Ra_1 \propto A_+$ and $Ra_3 \propto A_-$, where A_+ and A_- are specific reaction areas in the positive electrode and negative electrode, respectively. In [18], $A_+ = A_{+max}\left(1-SOC^{\zeta}\right)$, $A_- = A_{-max}\left(1-SOC^{\zeta}\right)$ for charge, and $A_+ = A_{+max}SOC^{\zeta}$, $A_- = A_{-max}SOC^{\zeta}$ for discharge, therefore, $\frac{\lambda_{2c}}{\lambda_{4c}} = \frac{\lambda_{2d}}{\lambda_{4d}}$.

Let desired pole $\lambda_d = \lambda_{dd}$ for the discharge subsystem, and $\lambda_d = \lambda_{dc} = \gamma\lambda_{dd}$ for the charge subsystem, where $\gamma = \frac{\lambda_{2c}}{\lambda_{2d}} = \frac{\lambda_{4c}}{\lambda_{4d}}$,

we can obtain

$$\mathbf{\Lambda_1} = \mathbf{T}^{-1}\mathbf{A_{CL1}}\mathbf{T} = \begin{bmatrix} -\lambda_{dc} & 0 & 0 \\ 0 & -\lambda_{2c} & 0 \\ 0 & 0 & -\lambda_{4c} \end{bmatrix}$$

and

$$\mathbf{\Lambda_2} = \mathbf{T}^{-1}\mathbf{A_{CL2}}\mathbf{T} = \begin{bmatrix} -\lambda_{dd} & 0 & 0 \\ 0 & -\lambda_{2d} & 0 \\ 0 & 0 & -\lambda_{4d} \end{bmatrix}$$

by using transformation matrix

$$\mathbf{T} = \begin{bmatrix} 1 & \lambda_{dd} & 1 \\ \widetilde{U}_{PbO_2} & \widetilde{U}_{PbO_2}\lambda_{2d} & \widetilde{U}_{PbO_2} \\ 0 & 0 & -\widetilde{U}_{PbO_2}\left(1+\frac{\lambda_{4d}}{\lambda_{dd}}\right) \end{bmatrix}.$$

The error dynamics for subsystem i after equivalent transformation becomes

$$\dot{\widetilde{\mathbf{e}}} = \mathbf{\Lambda_i}\widetilde{\mathbf{e}},$$

where

$$\widetilde{\mathbf{e}} = \mathbf{T}^{-1}\mathbf{e}.$$

The Common Quadratic Lyapunov function $V = \widetilde{\mathbf{e}}^{\mathbf{T}}\widetilde{\mathbf{e}}$ is radially unbounded and decresent. Time derivative of V

$$\dot{V} = \begin{cases} 2\widetilde{\mathbf{e}}^T\mathbf{\Lambda}_1\widetilde{\mathbf{e}} & \sum(\mathbf{A}_1,\mathbf{B}_1,\mathbf{C}_1,\mathbf{D}_1) \text{ is active} \\ 2\widetilde{\mathbf{e}}^T\mathbf{\Lambda}_2\widetilde{\mathbf{e}} & \sum(\mathbf{A}_2,\mathbf{B}_2,\mathbf{C}_2,\mathbf{D}_2) \text{ is active} \end{cases}.$$

So $\dot{V} \leq 2\max\left\{\lambda_{max}\left(\mathbf{\Lambda}_1\right),\lambda_{max}\left(\mathbf{\Lambda}_2\right)\right\}\|\widetilde{\mathbf{e}}\|_2 \leq -\lambda V$, where

$$\lambda = -2\max\left\{\lambda_{max}\left(\mathbf{\Lambda}_1\right),\lambda_{max}\left(\mathbf{\Lambda}_2\right)\right\} > 0.$$

Hence, the switched linear error dynamics is exponentially stable.

Bibliography

[1] Bode, H. (1977) *Lead-acid batteries*, Wiley.

[2] Hejabi, M., A. Oweisi, and N. Gharib (2006) "Modeling of kinetic behavior of the lead dioxide electrode in a lead-acid battery by means of electrochemical impedance spectroscopy," *Journal of Power Sources*, **158**(2), pp. 944 – 948.

[3] Rahn, C. and C. Wang (2013) *Battery Systems Engineering*, Wiley.

[4] Vasebi, A., M. Partovibakhsh, and S. M. T. Bathaee (2007) "A novel combined battery model for state-of-charge estimation in lead-acid batteries based on extended Kalman filter for hybrid electric vehicle applications," *Journal of Power Sources*, **174**(1), pp. 30 – 40, hybrid Electric Vehicles.

[5] Ning, G. and B. N. Popov (2004) "Cycle Life Modeling of Lithium-Ion Batteries," **151**(10), pp. A1584–A1591.

[6] Smith, K. A., C. D. Rahn, and C.-Y. Wang (2007) "Control oriented 1D electrochemical model of lithium ion battery," *Energy Conversion and Management*, **48**(9), pp. 2565 – 2578.

[7] Gebhart, B. (1993) *Heat Conduction and Mass Diffusion*, McGraw-Hill, New York, NY.

[8] Santhanagopalan, S., Q. Guo, P. Ramadass, and R. E. White (2006) "Review of models for predicting the cycling performance of lithium ion batteries," *Journal of Power Sources*, **156**(2), pp. 620 – 628.

[9] Subramanian, V. R., J. A. Ritter, and R. E. White (2001) "Approximate Solutions for Galvanostatic Discharge of Spherical Particles I. Constant Diffusion Coefficient," *Journal of The Electrochemical Society*, **148**(11), pp. E444 – E449.

[10] Ritz, W. (1909) "uber eine neue Methode zur Losung gewisser Variationsprobleme der mathematischen Physik," *Journal fur die Reine und Angewandte Mathematik*, **135**, pp. 1 – 61.

[11] Reddy, J. and D. Gartling (2010) *The Finite Element Method in Heat Transfer and Fluid Dynamics, Third Edition*, CRC series in computational mechanics and applied analysis, Taylor and Francis.

[12] Hill, J. M. and J. N. Dewynne (1987) *Heat Conduction*, Blackwell Scientific Publications, Oxford.

[13] Ozisik, M. N. (1980) *Heat Conduction*, John Wiley and Sons, New York, NY.

[14] Shamash, Y. (1975) "Linear system reduction using Pade approximation to allow retention of dominant modes," *International Journal of Control*, **21**(2), pp. 257–272.

[15] Golub, G. and C. Van Loan (1996) *Matrix Computations*, Johns Hopkins Studies in the Mathematical Sciences, Johns Hopkins University Press.

[16] Srinivasan, V., G. Q. Wang, and C. Y. Wang (2003) "Mathematical Modeling of Current-Interrupt and Pulse Operation of Valve-Regulated Lead Acid Cells," *Journal of The Electrochemical Society*, **150**(3), pp. A316 – A325.

[17] Bernardi, D. M. and M. K. Carpenter (1995) "A Mathematical Model of the Oxygen-Recombination Lead-Acid Cell," *Journal of The Electrochemical Society*, **142**(8), pp. 2631 – 2642.

[18] Gu, W. B., C. Y. Wang, and B. Y. Liaw (1997) "Numerical Modeling of Coupled Electrochemical and Transport Processes in Lead-Acid Batteries," *Journal of The Electrochemical Society*, **144**(6), pp. 2053 – 2061.

[19] Gu, W. B., G. Q. Wang, and C. Y. Wang (2002) "Modeling the overcharge process of VRLA batteries," *Journal of Power Sources*, **108**, pp. 174 – 184.

[20] Newman, J. and W. Tiedemann (1975) "Porous-electrode theory with battery applications," *AIChE Journal*, **21**(1), pp. 25–41.

[21] Gu, H., T. V. Nguyen, and R. E. White (1987) "A Mathematical Model of a Lead-Acid Cell," *Journal of The Electrochemical Society*, **134**(12), pp. 2953 – 2960.

[22] Salameh, Z., M. Casacca, and W. Lynch (1992) "A mathematical model for lead-acid batteries," *Energy Conversion, IEEE Transactions on*, **7**(1), pp. 93 – 98.

[23] Ceraolo, M. (2000) "New dynamical models of lead-acid batteries," *Power Systems, IEEE Transactions on*, **15**(4), pp. 1184 –1190.

[24] Huggins, R. (1999) "General equivalent circuit of batteries and fuel cells," *Ionics*, **5**, pp. 269 – 274.

[25] Durr, M., A. Cruden, S. Gair, and J. McDonald (2006) "Dynamic model of a lead acid battery for use in a domestic fuel cell system," *Journal of Power Sources*, **161**(2), pp. 1400 – 1411.

[26] Shi, Y., G. Prasad, Z. Shen, and C. Rahn (2011) "Discretization methods for battery systems modeling," American Control Conference, San Francisco, California.

[27] Pop, V., H. Bergveld, D. Danilov, P. Regtien, and P. Notten (2008) *Battery management systems: accurate state-of-charge indication for battery powered applications*, Philips research book series, Springer.

[28] Piller, S., M. Perrin, and A. Jossen (2001) "Methods for state-of-charge determination and their applications," *Journal of Power Sources*, **96**(1), pp. 113 – 120, proceedings of the 22nd International Power Sources Symposium.

[29] Pop, V., H. J. Bergveld, P. H. L. Notten, and P. P. L. Regtien (2005) "State-of-the-art of battery state-of-charge determination," *Measurement Science and Technology*, **16**(12), p. R93.

[30] Ng, K. S., C.-S. Moo, Y.-P. Chen, and Y.-C. Hsieh (2009) "Enhanced coulomb counting method for estimating state-of-charge and state-of-health of lithium-ion batteries," *Applied Energy*, **86**(9), pp. 1506 – 1511.

[31] Plett, G. L. (2004) "Extended Kalman filtering for battery management systems of LiPB-based HEV battery packs: Part 1. Background," *Journal of Power Sources*, **134**(2), pp. 252 – 261.

[32] ——— (2004) "Extended Kalman filtering for battery management systems of LiPB-based HEV battery packs: Part 2. Modeling and identification," *Journal of Power Sources*, **134**(2), pp. 262 – 276.

[33] ——— (2004) "Extended Kalman filtering for battery management systems of LiPB-based HEV battery packs: Part 3. State and parameter estimation," *Journal of Power Sources*, **134**(2), pp. 277 – 292.

[34] Vasebi, A., S. Bathaee, and M. Partovibakhsh (2008) "Predicting state of charge of lead-acid batteries for hybrid electric vehicles by extended Kalman filter," *Energy Conversion and Management*, **49**(1), pp. 75 – 82.

[35] Santhanagopalan, S. and R. E. White (2006) "Online estimation of the state of charge of a lithium ion cell," *Journal of Power Sources*, **161**(2), pp. 1346 – 1355.

[36] Santhanagopalan, S. and R. White (2008) "State of charge estimation for electrical vehicle batteries," in *Control Applications, 2008. CCA 2008. IEEE International Conference on*, pp. 690 – 695.

[37] Santhanagopalan, S. and R. E. White (2010) "State of charge estimation using an unscented filter for high power lithium ion cells," *International Journal of Energy Research*, **34**(2), pp. 152 – 163.

[38] Shen, Z., J. Gou, C. D. Rahn, and C.-Y. Wang (2011) "Ritz Model of a Lead-Acid Battery With Application to Electric Locomotives," *ASME Conference Proceedings*, **2011**(54754), pp. 713–720.

[39] Ge, S. and Z. Sun (2005) *Switched linear systems: Control and design*, Communications and control engineering series, Springer.

[40] Lin, H. and P. Antsaklis (2009) "Stability and Stabilizability of Switched Linear Systems: A Survey of Recent Results," *Automatic Control, IEEE Transactions on*, **54**(2), pp. 308 – 322.

[41] Alessandri, A., M. Baglietto, and G. Battistelli (2005) "Luenberger Observers For Switching Discrete-Time Linear Systems," in *Decision and Control, 2005 and 2005 European Control Conference. CDC-ECC '05. 44th IEEE Conference on*, pp. 7014 – 7019.

[42] Berndt, D., E. Meissner, and W. Rusch (1993) "Aging effects in valve-regulated lead-acid batteries," in *Telecommunications Energy Conference, INTELEC '93. 15th International*, vol. 2, pp. 139 –145 vol.2.

[43] Ruetschi, P. (2004) "Aging mechanisms and service life of leadCacid batteries," *Journal of Power Sources*, **127**(1C2), pp. 33 – 44.

[44] Blanke, H., O. Bohlen, S. Buller, R. W. D. Doncker, B. Fricke, A. Hammouche, D. Linzen, M. Thele, and D. U. Sauer (2005) "Impedance measurements on leadCacid batteries for state-of-charge, state-of-health and cranking capability prognosis in electric and hybrid electric vehicles," *Journal of Power Sources*, **144**(2), pp. 418 – 425.

[45] Okoshi, T., K. Yamada, T. Hirasawa, and A. Emori (2006) "Battery condition monitoring (BCM) technologies about leadCacid batteries," *Journal of Power Sources*, **158**(2), pp. 874 – 878.

[46] Delaille, A., M. Perrin, F. Huet, and L. Hernout (2006) "Study of the coup de fouet of lead-acid cells as a function of their state-of-charge and state-of-health," *Journal of Power Sources*, **158**(2), pp. 1019 – 1028.

[47] de Oliveira, C. and M. Lopes (2004) "Early stages of the lead-acid battery discharge," *Journal of Power Sources*, **138**(1C2), pp. 294 – 300.

[48] Bose, C. and F. Laman (2000) "Battery state of health estimation through coup de fouet," in *Telecommunications Energy Conference, 2000. INTELEC. Twenty-second International*, pp. 597–601.

[49] Pascoe, P., H. Sirisena, and A. Anbuky (2002) "Coup de fouet based VRLA battery capacity estimation," in *Electronic Design, Test and Applications, 2002. Proceedings. The First IEEE International Workshop on*, pp. 149–153.

[50] Gould, C., C. Bingham, D. Stone, and P. Bentley (2009) "New Battery Model and State-of-Health Determination Through Subspace Parameter Estimation and State-Observer Techniques," *Vehicular Technology, IEEE Transactions on*, **58**(8), pp. 3905 –3916.

[51] Ljung, L. (1998) *System Identification: Theory for the User*, Pearson Education.

[52] Bhangu, B., P. Bentley, D. Stone, and C. Bingham (2005) "Nonlinear observers for predicting state-of-charge and state-of-health of lead-acid batteries for hybrid-electric vehicles," *Vehicular Technology, IEEE Transactions on*, **54**(3), pp. 783 – 794.

[53] Shahriari, M. and M. Farrokhi (2010) "State of health estimation of VRLA batteries using fuzzy logic," in *Electrical Engineering (ICEE), 2010 18th Iranian Conference on*, pp. 629–634.

[54] Prasad, G. K. and C. D. Rahn (2013) "Model based identification of aging parameters in lithium ion batteries," *Journal of Power Sources*, **232**(0), pp. 79 – 85.

[55] Sastry, S. and M. Bodson (2011) *Adaptive Control: Stability, Convergence and Robustness*, Dover Books on Electrical Engineering Series, Dover Publications.

[56] Prasad, G. K. and C. D. Rahn (2012) "Development of a First Principles Equivalent Circuit Model for a Lithium ion Battery," *ASME Conference Proceedings*.

[57] Shaju, K., G. S. Rao, and B. Chowdari (2004) "Influence of Li-Ion Kinetics in the Cathodic Performance of Layered $Li(Ni_{\frac{1}{3}}Co_{\frac{1}{3}}Mn_{\frac{1}{3}})O_2$," *Journal of The Electrochemical Society*, **151**(9), pp. A1324–A1332.

[58] Levi, M. and D. Aurbach (1997) "Diffusion coefficients of lithium ions during intercalation into graphite derived from the simultaneous measurements and modeling of electrochemical impedance and potentiostatic intermittent titration characteristics of thin graphite electrodes," *The Journal of Physical Chemistry B*, **101**(23), pp. 4641–4647.

[59] Guyomard, D. and J. Tarascon (1992) "Li Metal-Free Rechargeable LiMn2 O 4/Carbon Cells: Their Understanding and Optimization," *Journal of The Electrochemical Society*, **139**(4), pp. 937–948.

[60] Backholm, J., P. Georén, and G. A. Niklasson (2008) "Determination of solid phase chemical diffusion coefficient and density of states by electrochemical methods: Application to iridium oxide-based thin films," *Journal of Applied Physics*, **103**(2), pp. 023702–023702.

[61] Weppner, W. and R. A. Huggins (1977) "Determination of the Kinetic Parameters of Mixed-Conducting Electrodes and Application to the System Li3Sb," *Journal of The Electrochemical Society*, **124**(10), pp. 1569–1578.

[62] Wang, Q., H. Li, X. Huang, and L. Chen (2001) "Determination of chemical diffusion coefficient of lithium ion in graphitized mesocarbon microbeads with potential relaxation technique," *Journal of The Electrochemical Society*, **148**(7), pp. A737–A741.

[63] Zhu, Y. and C. Wang (2010) "Galvanostatic intermittent titration technique for phase-transformation electrodes," *The Journal of Physical Chemistry C*, **114**(6), pp. 2830–2841.

[64] Yu, P., B. N. Popov, J. A. Ritter, and R. E. White (1999) "Determination of the lithium ion diffusion coefficient in graphite," *Journal of The Electrochemical Society*, **146**(1), pp. 8–14.

[65] Funabiki, A., M. Inaba, and Z. Ogumi (1997) "Ac impedance analysis of electrochemical lithium intercalation into highly oriented pyrolytic graphite," *Journal of power sources*, **68**(2), pp. 227–231.

[66] Nicholson, R. S. (1965) "Theory and Application of Cyclic Voltammetry for Measurement of Electrode Reaction Kinetics." *Analytical Chemistry*, **37**(11), pp. 1351–1355.

[67] Vielstich, W. (2010) *Cyclic voltammetry*, Wiley Online Library.

[68] Rui, X., N. Ding, J. Liu, C. Li, and C. Chen (2010) "Analysis of the chemical diffusion coefficient of lithium ions in $Li_3V_2(PO_4)_3$ cathode material," *Electrochimica Acta*, **55**(7), pp. 2384–2390.

[69] Boyd, S., L. Ghaoul, E. Feron, and V. Balakrishnan (1994) *Linear Matrix Inequalities in System and Control Theory*, Siam Studies in Applied Mathematics, Society for Industrial and Applied Mathematics.

[70] Bard, A. J. and L. R. Faulkner (2001) *Electrochemical methods: fundamentals and applications*, John Wiley and Sons, New York, NY.

[71] Shi, Y., C. Ferone, C. Rao, and C. Rahn (2012) "Nondestructive Forensic Pathology of Lead-Acid Batteries," American Control Conference, Montreal, Canada.

[72] Polyak, B. T. and P. S. Shcherbakov (2002) "Superstable Linear Control Systems. II. Design," *Automation and Remote Control*, **63**, pp. 1745–1763.

[73] Alessandri, A. and P. Coletta (2001) "Switching observers for continuous-time and discrete-time linear systems," in *American Control Conference, 2001. Proceedings of the 2001*, vol. 3, pp. 2516 –2521 vol.3.

[74] Ko, H.-S., J. Jatskevich, G. Dumont, and G.-G. Yoon (2008) "An advanced LMI-based-LQR design for voltage control of grid-connected wind farm," *Electric Power Systems Research*, **78**(4), pp. 539 – 546.

[75] Zhang, F. (2005) *The Schur Complement and Its Applications*, Numerical Methods and Algorithms, Springer.

[76] Connors, K. (1990) *Chemical Kinetics: The Study of Reaction Rates in Solution*, VCH.

[77] Ferone, C. (2012) Master's thesis, The Pennsylvania State University.

[78] Guo, M., G. Sikha, and R. E. White (2011) "Single-Particle Model for a Lithium-Ion Cell: Thermal Behavior," **158**(2), pp. A122–A132.

[79] Srinivasan, V. and J. Newman (2004) "Discharge model for the lithium iron-phosphate electrode," *Journal of The Electrochemical Society*, **151**(10), pp. A1517–A1529.

[80] Lee, Y.-S. and M.-W. Cheng (2005) "Intelligent control battery equalization for series connected lithium-ion battery strings," *Industrial Electronics, IEEE Transactions on*, **52**(5), pp. 1297 – 1307.

[81] Cao, J., N. Schofield, and A. Emadi (2008) "Battery balancing methods: A comprehensive review," in *Vehicle Power and Propulsion Conference, 2008. VPPC '08. IEEE*, pp. 1 –6.

[82] Xie, W. and Y. Xia (2011) "Data-driven method for Kalman filtering," in *Intelligent Control and Information Processing (ICICIP), 2011 2nd International Conference on*, vol. 2, IEEE, pp. 830–835.

[83] Goldberg, D. E. and J. H. Holland (1988) "Genetic algorithms and machine learning," *Machine learning*, **3**(2), pp. 95–99.

[84] Watkins, C. J. and P. Dayan (1992) "Q-learning," *Machine learning*, **8**(3-4), pp. 279–292.

[85] Landau, Y. D. (1979) *Adaptive control: the model reference approach*, IET.

[86] Bellman, R. (1961) *Adaptive control processes: a guided tour*, vol. 4, Princeton university press Princeton.

[87] Rao, C., A. Ray, S. Sarkar, and M. Yasar (2009) "Review and comparative evaluation of symbolic dynamic filtering for detection of anomaly patterns," *Signal, Image and Video Processing*, **3**(2), pp. 101–114.

[88] Ray, A. (2004) "Symbolic dynamic analysis of complex systems for anomaly detection," *Signal Processing*, **84**(7), pp. 1115–1130.

[89] Gupta, S., A. Ray, and A. Mukhopadhyay (2006) "Anomaly detection in thermal pulse combustors using symbolic time series analysis," *Proceedings of the Institution of Mechanical Engineers, Part I: Journal of Systems and Control Engineering*, **220**(5), pp. 339–351.

[90] Gupta, S., A. Ray, and E. Keller (2007) "Symbolic time series analysis of ultrasonic data for early detection of fatigue damage," *Mechanical Systems and Signal Processing*, **21**(2), pp. 866–884.

Vita

Zheng Shen

EDUCATION

2009 - 2013, *Pennsylvania State University, University Park, PA*
Ph.D. Mechanical Engineering, Electrical Engineering (Minor).

2008 - 2009, *University of Michigan, Ann Arbor, MI*
M.S.E. Mechanical Engineering.

2003 - 2007, *Shanghai Jiao Tong University, Shanghai, China*
B.S.E. Mechanical Engineering, International Economy and Trade (Minor).

WORK EXPERIENCE

Jan 2010 - Aug 2013, **Graduate Research Assistant**
Mechatronics Research Lab, Pennsylvania State University.

Aug 2009 - Dec 2009, **Graduate Teaching Assistant**
Department of Mechanical and Nuclear Engineering, Pennsylvania State University.

Aug 2008 - May 2009, **Graduate Research Assistant**
S.M. Wu Manufacturing Research Center (WuMRC), University of Michigan.

Aug 2007 - Jul 2008, **Graduate Research Assistant**
State Key Lab of Mechanical System and Vibration, Shanghai Jiao Tong University.

PROFESSIONAL AFFILIATIONS

Student Member, American Society of Mechanical Engineers.